



저작자표시-비영리-변경금지 2.0 대한민국

이용자는 아래의 조건을 따르는 경우에 한하여 자유롭게

- 이 저작물을 복제, 배포, 전송, 전시, 공연 및 방송할 수 있습니다.

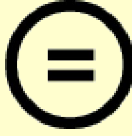
다음과 같은 조건을 따라야 합니다:



저작자표시. 귀하는 원저작자를 표시하여야 합니다.



비영리. 귀하는 이 저작물을 영리 목적으로 이용할 수 없습니다.



변경금지. 귀하는 이 저작물을 개작, 변형 또는 가공할 수 없습니다.

- 귀하는, 이 저작물의 재이용이나 배포의 경우, 이 저작물에 적용된 이용허락조건을 명확하게 나타내어야 합니다.
- 저작권자로부터 별도의 허가를 받으면 이러한 조건들은 적용되지 않습니다.

저작권법에 따른 이용자의 권리는 위의 내용에 의하여 영향을 받지 않습니다.

이것은 [이용허락규약\(Legal Code\)](#)을 이해하기 쉽게 요약한 것입니다.

[Disclaimer](#)

Thesis for the Degree of Master of Science

**Synthesis and Physicochemical  
Characterization of Metal (Zr, Ti, Zn,  
Mo) Oxide**



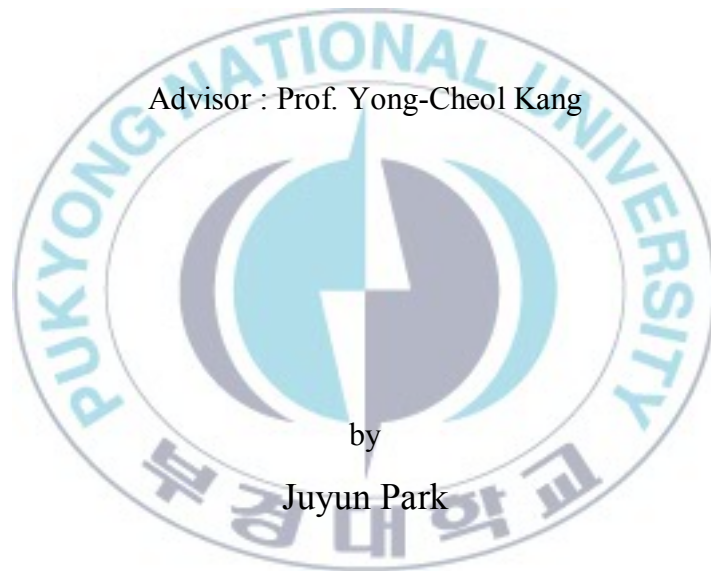
by

Juyun Park

Department of Chemistry  
The Graduate School  
Pukyong National University  
February 2010

**Synthesis and Physicochemical  
Characterization of Metal (Zr, Ti, Zn,  
Mo) Oxide**

(금속 (Zr, Ti, Zn, Mo) 산화물의 합성과  
물리화학적 분석)



Advisor : Prof. Yong-Cheol Kang

by

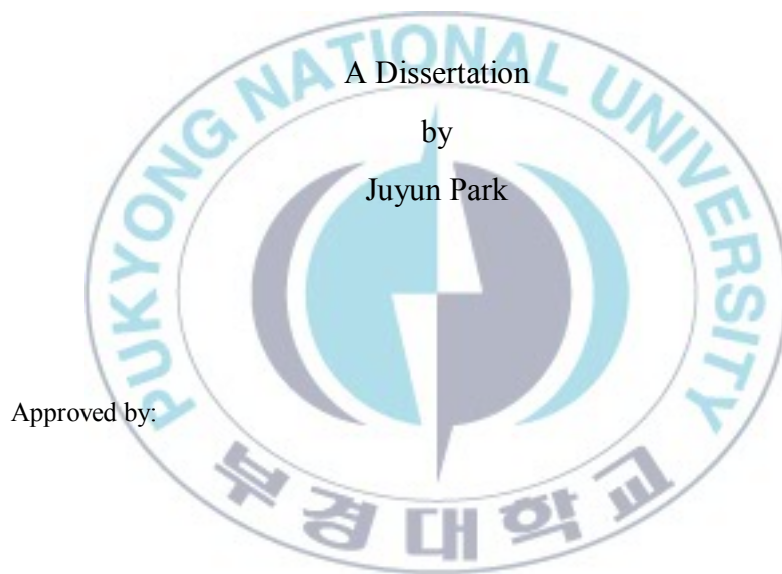
Juyun Park

A thesis submitted in partial fulfillment of the requirements  
for the degree of  
Master of Science

in Department of Chemistry, The Graduate School,  
Pukyong National University

February 2010

**Synthesis and Physicochemical Characterization of  
Metal (Zr, Ti, Zn, Mo) Oxide**



---

(Chairman) : Ju Chang Kim

---

(Member) : Sang Yong Pyun

---

(Member) : Yong-Cheol Kang

February 25, 2010

# CONTENTS

<b>LIST OF FIGURES</b> .....	iv
<b>LIST OF TABLES</b> .....	xi
<b>ABSTRACT</b> .....	xii
<b>CHAPTER 1. Theories</b> .....	1
<b>1.1. Temperature Programmed Desorption (TPD)</b> .....	1
<b>1.2. Auger Electron Spectroscopy (AES)</b> .....	5
<b>1.3. X-ray Photoelectron Spectroscopy (XPS)</b> .....	7
<b>1.4. References</b> .....	11
<b>CHAPTER 2. Behavior of C<sub>2</sub>D<sub>5</sub>OD on Zircaloy-4 Surfaces</b> .....	12
<b>2.1. Introduction</b> .....	12
<b>2.2. Experimental Section</b> .....	13
<b>2.3. Results and Discussion</b> .....	17
<b>2.3.1. Temperature Programmed Desorption:</b>	
C <sub>2</sub> D <sub>5</sub> OD/Zircaloy-4 .....	17
<b>2.3.2. Auger Electron Spectroscopy:</b>	
C <sub>2</sub> D <sub>5</sub> OD/Zircaloy-4 .....	20
<b>2.4. Conclusion</b> .....	25
<b>2.5. References</b> .....	26

<b>CHAPTER 3. Characterization of Nanofibers Synthesized by</b>	
<b>Electrospinning</b> .....	29
<b>3.1. Characterization of Titania Doped Nanofibers</b> .....	29
3.1.1. Introduction .....	29
3.1.2. Experimental Section .....	30
3.1.3. Results and Discussion .....	33
3.1.4. Conclusion .....	38
<b>3.2. Structural, Electrical, and Optical Properties of</b>	
<b>Aluminum Oxide Doped Zinc Oxide (AOZO)</b>	
<b>Nanofibers</b> .....	39
3.2.1. Introduction .....	39
3.2.2. Experimental Section .....	40
3.2.3. Results and Discussion .....	43
3.2.4. Conclusion .....	52
<b>3.3. References</b> .....	53
<b>CHAPTER 4. Investigation of Thin films</b> .....	58
<b>4.1. XPS Investigation of Molybdenum Thin Films</b> .....	58
4.1.1. Introduction .....	58
4.1.2. Experimental Section .....	59
4.1.3. Results and Discussion .....	60
4.1.4. Conclusion .....	67
<b>4.2. Properties of Zirconium Oxide Thin Films with Different</b>	
<b>Plasma Gas Ratio</b> .....	68
4.2.1. Introduction .....	68
4.2.2. Experimental Section .....	69
4.2.3. Results and Discussion .....	71

4.2.4. Conclusion .....	79
4.3. References .....	80
<b>KOREAN ABSTRACT .....</b>	<b>84</b>
<b>ACKNOWLEDGMENTS .....</b>	<b>86</b>



## LIST OF FIGURES

Figure 1.1.	Schematic drawing of the TPD experiment.	2
Figure 1.2.	(a) zeroth-order desorption kinetics, (b) first-order desorption kinetics, (c) second-order desorption kinetics.	5
Figure 1.3.	Illustration of the production process for $KL_1L_{2,3}$ Auger electrons, (a) K level is ionized by incident electron beam, (b) K level is filled by an $L_1$ level electron, (c) the energy ( $E_K - E_{L1}$ ) used to remove another electron ( $KL_1L_{2,3}$ Auger electron) from the $L_{2,3}$ level.	7
Figure 1.4.	Schematic diagram of the XPS process.	8
Figure 2.1.	Purity of DE checked with the QMS. The bottom line shows the background of the analysis chamber. The top line was taken after purified DE backfilled into the chamber. Even pure deuterized ethanol was used for this work, hydrogen exchange could be occurred in the gas handling system. This caused by $H_2^+$ peak at 2 amu.	16

- Figure 2.2. Temperature programmed desorption spectra of (a) 2 amu and (b) 4 amu following DE adsorption on Zircaloy-4 at 190 K. The numbers in the figure represent the exposure in langmuir unit. The notations used in the title of these figures, such as H<sub>2</sub>/C<sub>2</sub>D<sub>5</sub>OD/Zry-4, means H<sub>2</sub> evolution after DE dosed on the Zry-4 surfaces. 18
- Figure 2.3. Temperature programmed desorption spectra of (a) 20 amu and (b) 28 amu following DE adsorption on Zircaloy-4 at 190 K. 20
- Figure 2.4. Derivative mode of Auger electron spectra of the survey scan of Zircaloy-4. 21
- Figure 2.5. (a) Auger electron spectra of the Zr features including Zr(MNN), Zr(MNV)<sub>o</sub>, Zr(MNV)<sub>m</sub>, and Zr(MVV), (b) AES of the C(KLL, 270 eV) peak, and (c) AES spectra of the O(KLL, 510 eV). The vertical lines in the figures were put to see the shift of peak clearly. 23
- Figure 2.6. Auger peak-to-peak heights (APPH) ratio versus annealing temperature. Filled circles represent for C(KLL)/Zr(MNV)<sub>m</sub> and hollow triangles represent for O(KLL)/Zr(MNV)<sub>m</sub>. The data inside of the 25

circle bottom of the left in the figure present APPH ratios of C/Zr and O/Zr of the clean Zry-4 surface.

- Figure 3.1. The schematic diagram of XPS chamber (VG ESCALAB MK II). 33
- Figure 3.2. Scanning electron microscopy (SEM) images of, 34  
(a) titania sol-coated nylon fibers calcined at 120°C, and (b) calcined at 350°C.
- Figure 3.3. DRIFT spectra from titania-coated Nylon-6 35  
nanofiber mats after heating to (a) anatase-120°C, (b) anatase-275°C, (c) anatase-350°C, and (d) rutile-700°C (A = anatase and R = rutile).
- Figure 3.4. XRD spectra for (a) anatase titania nanofibers 36  
calcined at 350°C and (b) rutile titania fibers calcined at 700°C.
- Figure 3.5. High resolution XP spectra of the Ti 2p region (a) 38  
and valence band region (b) comparing rutile and anatase titania (A = anatase, R = rutile, A-R = subtraction of rutile XPS intensity from anatase XPS intensity).
- Figure 3.6. Representative SEM image of aluminum oxide 44  
doped zinc oxide nanofibers (sample AOZO1)

exhibiting an average fiber diameter 100 nm after being calcined at 873 K for 5 hrs.

- Figure 3.7. XRD patterns of undoped and aluminum oxide doped zinc oxide nanofibers calcined at 873 K for 5 hrs. 45
- Figure 3.8. Crystallite size of zinc oxide nanofibers at different concentration of aluminum (in the electrospinning solution). 46
- Figure 3.9. UV-Vis spectra of undoped and aluminum oxide doped zinc oxide nanofibers (calcined at 873 K for 5 hrs). 47
- Figure 3.10. Electrical conductivities of undoped and aluminum oxide doped zinc oxide nanofibers (calcined at 873 K for 5 hrs). 49
- Figure 3.11. High resolution X-ray photoelectron spectra from undoped zinc oxide to AOZO3 of the Zn 2p region (a), O 1s region (b), and Al 2s region (c) from bottom to top. 50
- Figure 3.12. Representative deconvoluted X-ray photoelectron spectra AOZO1(bottom) and AOZO3(top) of the Zn 2p<sub>3/2</sub> region (a), O 1s region (b), and Al 2s region (c). In (a) metallic zinc at a binding energy

of 1021.5 eV and zinc oxide at around 1022.8 eV are assigned. In (b) the assigned binding energies for oxygen are around 530.3 eV for ZnO, 531.5 eV for low binding energy aluminum oxide ( $\text{AlO}_x$ ), 532.2 eV for surface hydroxide, and 533.7 eV for high binding energy aluminum oxide ( $\text{AlO}_y$ ). In (c) metallic aluminum at 119.4 eV, low binding energy aluminum oxide at 119.9 eV, and high binding energy aluminum oxide at 121.0 eV denoted  $\text{Al}^0$ ,  $\text{AlO}_x$ , and  $\text{AlO}_y$  (where  $x < y$ ) are indicated.

Figure 4.1. Survey scans of sputter deposited Mo thin films. 61  
The notations are Mo-1 for deposition at 4 mTorr, Mo-2 for 8 mTorr, Mo-3 for 12 mTorr, Mo-4 for 16 mTorr, and Mo-5 for 20 mTorr working pressure in the RF magnetron sputtering chamber.

Figure 4.2. High resolution XP spectra of the Mo 3d range of 62  
Mo thin films. Mo 3d XP spectra of five different samples are stacked in figure (a). Deconvoluted spectra of three representative samples are shown in figure (b). In Figure (b), **1**, **2**, and **3** denote metallic Mo ( $\text{Mo}^0$ ),  $\text{Mo}^{4+}$ , and

Mo<sup>6+</sup>, respectively.

- Figure 4.3. High resolution XP spectra of the O 1s range of Mo thin films. O 1s XP spectra of five different samples are stacked in Figure (a). Deconvoluted spectra of three representative samples are shown in figure (b). In figure (b), 1, 2, and 3 denote oxygen environments assigned to O-Mo<sup>6+</sup>, O-Mo<sup>4+</sup>, and surface oxygen, respectively. 63
- Figure 4.4. High resolution XP spectra of the Na 1s range of Mo thin films. Na 1s XP spectra of five different samples are stacked in Figure (a). Deconvoluted spectra of three representative samples are shown in figure (b). 64
- Figure 4.5. Atomic percentages of each element in the surface region of the Mo deposited thin films; molybdenum in (a), oxygen in (b), and sodium in (c). 65
- Figure 4.6. Atomic percentages of each chemical species of oxygen and molybdenum in (a) and (b), respectively. 66
- Figure 4.7. The thickness of the zirconium oxide thin films with different percentage of O<sub>2</sub> in the sputter gas. 72

- Figure 4.8. The XRD patterns of the zirconium oxide thin films on Si(100). The notation of the thin films is represented by O<sub>2</sub>-number. In O<sub>2</sub>-4, the number 4 indicates that the O<sub>2</sub> gas flow rate was 4 sccm and the total gas flow rate (O<sub>2</sub>+Ar) was constant at 20 sccm. 74
- Figure 4.9. (a) Zr 3d and (b) O 1s XP spectra of zirconium oxide thin films prepared at different O<sub>2</sub> concentration. 75
- Figure 4.10. Deconvoluted XP spectra of Zr 3d: O<sub>2</sub>-16 (a), O<sub>2</sub>-10 (b), and O<sub>2</sub>-0 (c) and O 1s: O<sub>2</sub>-16 (d), O<sub>2</sub>-10 (e), and O<sub>2</sub>-0 (f). 77
- Figure 4.11. The relative ratios of (a) Zr species and (b) O species of different percentage of O<sub>2</sub> in sputter gas. 79

## LIST OF TABLES

Table 1.	The comparison of y-axis, slope, and intercept parameters depending on the desorption kinetics. The x-axis is $1/RT$ .	5
Table 2.	Atomic and X-ray notation.	10
Table 3.	Metallic elemental compositions of the four different aluminum oxide doped zinc oxide (AOZO) nanofiber samples after calcining at 873 K for 5 hrs.	41
Table 4.	The micro-structural parameters of the four different nanofiber samples.	46
Table 5.	Optical bandgap and conductivity of four different aluminum oxide doped zinc oxide (AOZO) nanofiber samples after calcining at 873 K for 5 hrs.	48
Table 6.	The deposition parameters for RF sputtered zirconium oxide thin films.	70

# Synthesis and Physicochemical Characterization of Metal (Zr, Ti, Zn, Mo) Oxide

Juyun Park

Department of Chemistry, Graduate School,  
Pukyong National University

## Abstract

Deuterized ethanol exposed Zircaloy-4 (Zry-4) surfaces with various amount of  $C_2D_5OD$  exposures at 190 K were investigated. In TPD study,  $D_2$  was evolved at two different desorption temperature regions, the lower temperature feature at around 520 K showed first-order desorption kinetics. The high temperature desorption peak at around 650 K was shifted to lower desorption temperature as the exposure of  $C_2D_5OD$  increased. The  $Zr(MNV)_o$  (oxide) peak revealed that metallic zirconium was oxidized by deuterized ethanol adsorption. After stepwise annealing of the oxidized Zry-4 sample up to 843 K, the  $Zr(MNV)_o$  (oxide) peak was gradually decreased and the  $Zr(MNV)_m$  (metallic) peak is increased. After the sample was heated to 843 K, the oxygen content near the Zry-4 surface was recovered to clean surface level. The concentration of carbon, however, was not recovered by annealing the sample.

Titania nanofibers were synthesized by sol-gel coating of electrospun polymer nanofibers followed by calcining to form either the pure anatase or rutile phases. The average diameter of these ceramic nanofibers was observed to be around 200 nm for both the rutile and anatase forms. The valence band structure is different, however, the binding energy of Ti 2p is constant.

Zinc oxide nanofibers doped with aluminum oxide were prepared by sol-gel processing and electrospinning techniques. The nanofibers had diameters in the range of 60~150nm. The incorporation of aluminum oxide resulted in a decrease in the crystallite sized of the zinc oxide nanofibers. Aluminum oxide doped zinc oxide (AOZO) nanofibers exhibited lower bandgap energies compared to undoped zinc oxide nanofibers. However, as the aluminum

content was increased from 1.70 at.% to 3.20 at.% in the electrospinning solution, the bandgap energy increased resulting in lower conductivity. The electrical conductivity of the AOZO samples was found to depend on the amount of aluminum dopant in the matrix as reflected in the changes in oxidation state elucidated from XPS data.

Sputter deposited Mo thin films on soda-lime glass are studied by X-ray photoelectron spectroscopy. It is found that the proportion of metallic Mo at the surface decreases and the number of Mo<sup>6+</sup> species increases as the Ar gas pressure used for sputtering is increased. Sodium, sputtered from the substrate, is also detected on the surface of the Mo thin films.

The surface behavior of zirconium oxide deposited Si(100) substrate depending on the different percentage of O<sub>2</sub> in sputter gas is investigated by X-ray photoelectron spectroscopy (XPS) for study about the chemical environment of the elements, X-ray diffraction (XRD) for check the crystallinity of the films, spectroscopic ellipsometry (SE) technique for measuring the thickness of the films, atomic force microscope (AFM) for the morphology of the thin films. The zirconium oxide thin film was deposited on the Si(100) surfaces applying radio-frequency (RF) magnetron sputtering process successfully. The monoclinic ZrO<sub>2</sub> and  $\alpha$ -Zr crystal structure were observed, and decrease of the thickness is about 10 nm with increasing O<sub>2</sub> concentration. The oxidation states of Zr 3d were changed from metal state to oxide state.

## CHAPTER 1. Theories

### 1.1. Temperature Programmed Desorption (TPD)

Temperature programmed desorption (TPD), also known as thermal desorption spectroscopy (TDS), is useful method for investigation of surface phenomena about kinetic and thermodynamic parameters of desorption processes or decomposition reactions. The sample surface is exposed to a certain gas to adsorb gas atoms or molecules at low temperature and adsorbed molecules bound to surface with the activation energy of desorption. As the sample is heated slowly and linearly, gas atoms and molecules will desorb from the surface at any one temperature. TPD is measured of the partial pressures of desorbing gases of adsorbed molecules by mass spectrometer with respect to the time. A schematic drawing of the TPD experiment is shown in Figure 1.1.

TPD spectra show following information [1]:

- The maximum temperature of the peak is related to the activation energy of desorption. When the temperature is higher, the molecules is adsorbed strongly onto the surface.
- The shape of the peak gives information about desorption kinetics, e.g. desorption order.
- The area under the peak is proportional to the surface coverage.

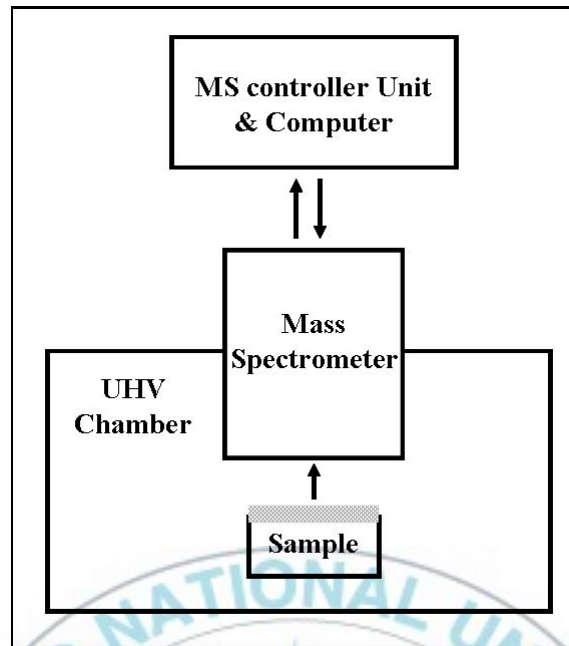


Figure 1.1. Schematic drawing of the TPD experiment.

The rate of desorption is in general expressed by the Polanyi-Wigner equation:

$$r_{des} = -\frac{d\Theta}{dt} = \nu \cdot \Theta^n \cdot \exp\left(-\frac{\Delta E_{des}}{RT}\right) \quad (1)$$

where  $r_{des}$  is the rate of desorption,  $\nu$  is the pre-exponential factor,  $\Theta$  is the coverage,  $n$  is the desorption (or kinetic) order,  $E_{des}$  is the activation energy of desorption,  $R$  is the gas constant, and  $T$  is the absolute temperature.

During TPD experiment, the temperature is increased linearly with time:

$$T(t) = T_0 + \frac{dT}{dt}t = T_0 + \beta t \quad (2)$$

where  $T_0$  is initial temperature,  $\beta$  is the heating rate ( $\text{K}\cdot\text{s}^{-1}$ ).

Inserting the time,  $t$ , in the Polanyi-Wigner equation by  $\frac{1}{dt} = \frac{\beta}{dT}$ :

$$r_{des} = -\frac{d\Theta}{dT} = \frac{v \cdot \Theta^n}{\beta} \cdot \exp\left(-\frac{\Delta E_{des}}{RT}\right) \quad (3)$$

The rate of desorption depends on the coverage ( $\Theta^n$ ) and energy term  $\left(-\frac{\Delta E_{des}}{RT}\right)$ .

The three reaction types of desorption order ( $n = 0, 1, 2$ ) are shown in Figure 1.2, schematically. In the zeroth-order desorption kinetics, it usually observed in multilayers. According to the equation (4), the rate of desorption does not depend on the coverage. The peaks in the zeroth-order desorption kinetics have a common leading edge which spectra starting with different coverages coincide in the ascending portion. When all adsorbed molecules have desorbed, the rate of desorption rapidly drops to zero [2,3].

$$r_{des} = -\frac{d\Theta}{dT} = \frac{v}{\beta} \cdot \exp\left(-\frac{\Delta E_{des}}{RT}\right) \quad (4)$$

When the desorption order is first, the rate of desorption is proportional to the coverage as seen in equation (5), but the maximum temperature of desorption is dependent of the  $\Delta E_{des}$ , not the coverage. The shape of the spectra is asymmetric with respect to the maximum temperature of desorption.

$$r_{des} = -\frac{d\Theta}{dT} = \frac{\nu \cdot \Theta}{\beta} \cdot \exp\left(-\frac{\Delta E_{des}}{RT}\right) \quad (5)$$

For the second-order desorption, the two adsorbed species are recombined on the surface, thus the second-order desorption occurred in the monolayer. The maximum temperature moves to lower temperature with coverage and the other characteristic mark is nearly symmetric peak shape.

$$r_{des} = -\frac{d\Theta}{dT} = \frac{\nu \cdot \Theta^2}{\beta} \cdot \exp\left(-\frac{\Delta E_{des}}{RT}\right) \quad (6)$$

From the equation (3), we can obtain the logarithm equation which give the values of activation energy and pre-exponential factor. In the plot of  $\ln\left(\frac{d\Theta}{dT}\right)$  (zeroth-order desorption kinetic) or  $\ln\left(\frac{T_{max}^2}{\beta}\right)$  (first and second-order desorption kinetics) versus  $\frac{1}{RT_{max}}$ , the slope is corresponding to  $\Delta E_{des}$  and the intercept is determined by  $\nu$ , as summarized in Table 1.

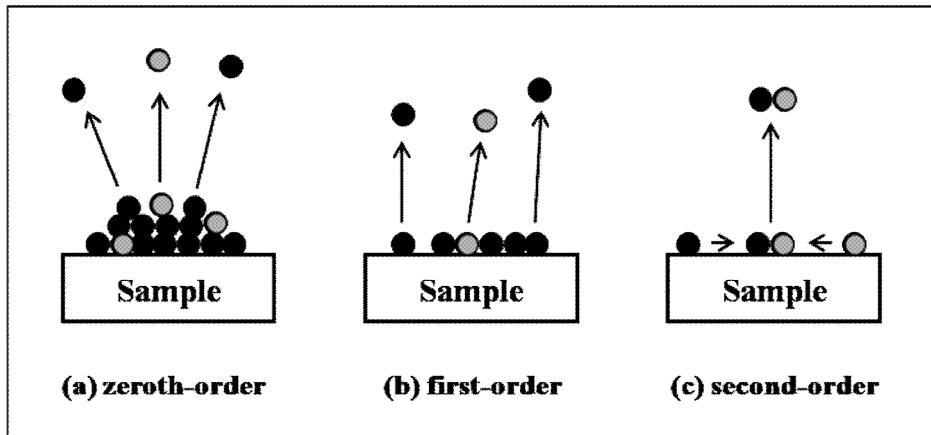


Figure 1.2. (a) zeroth-order desorption kinetics, (b) first-order desorption kinetics, (c) second-order desorption kinetics.

Table 1. The comparison of y-axis, slope, and intercept parameters depending on the desorption kinetics. The x-axis is  $1/RT$ .

condition	y-axis	slope	intercept
zeroth-order	$\ln\left(\frac{d\Theta}{dT}\right)$	$-\Delta E_{des}$	$\ln\left(\frac{v}{\beta}\right)$
first-order	$\ln\left(\frac{T_{max}^2}{\beta}\right)$	$\Delta E_{des}$	$\ln\left(\frac{\Delta E_{des}}{v \cdot R}\right)$
second-order	$\ln\left(\frac{T_{max}^2}{\beta}\right)$	$\Delta E_{des}$	$\ln\left(\frac{\Delta E_{des}}{v \cdot R \cdot \Theta}\right)$

## 1.2. Auger Electron Spectroscopy (AES)

Auger electron spectroscopy (AES) is one of the basic experimental tools of surface chemistry because it provides identification and quantitative determination of elements, information of phenomena such as adsorption, desorption and diffusion from the bulk.

Emission of Auger electron is resulted by three steps involving three electrons as shown in Figure 1.3. When an electron from the core level of atom is ejected by the incident electron beam, the resultant vacancy can be immediately filled by another electron of higher energy level. The energy released from this transition causes the emission of another electron. And this electron is referred to as an Auger electron. The kinetic energy ( $E_k$ ) of the Auger electron is given by

$$E_k = E_K - E_{L_1} - E_{L_{2,3}} - \phi$$

The three levels involved in Auger electron production are used to designate the Auger transition. The first letter designates the shell containing the initial core hole, the second letter designates the shell containing the relaxing electron and the last letter designates the shell of the second electron vacancy. Therefore three electrons must take part in an Auger process, H and He atoms can not be detected in AES.

The Auger spectrum contains many background electrons such as core level ionization, low energy secondary electrons, and the Auger peaks appearing as small features on the spectrum. Therefore, the Auger spectrum usually plots differential energy distribution,  $\frac{dN(E)}{dE}$ , versus kinetic energy of the Auger electrons [4]. The position of the peaks is used to identify the elements and the peak-to-peak height represents a peak intensity which is

determined the concentrations of elements in the sample. Chemical shifts are also observed as a shift of the peak position and/or a change in the peak shape.

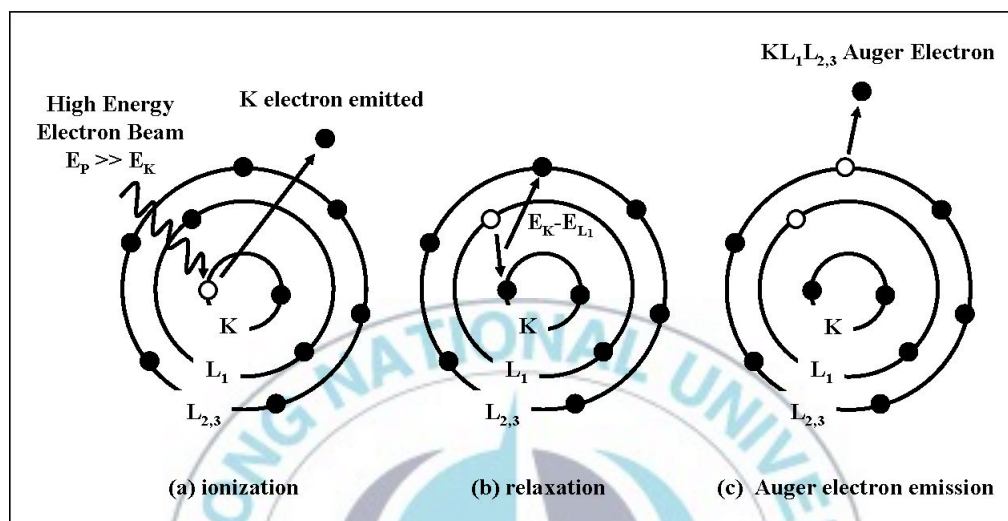


Figure 1.3. Illustration of the production process for  $KL_1L_{2,3}$  Auger electrons, (a) K level is ionized by incident electron beam, (b) K level is filled by an  $L_1$  level electron, (c) the energy ( $E_K - E_{L_1}$ ) used to remove another electron ( $KL_1L_{2,3}$  Auger electron) from the  $L_{2,3}$  level.

### 1.3. X-ray Photoelectron Spectroscopy (XPS)

X-ray photoelectron spectroscopy (XPS) is the most frequently used surface chemical technique for determining the elemental, chemical state, and electronic state of the elements in the sample. This technique is often also referred to as electron spectroscopy for chemical analysis (ESCA).

The theory of XPS is based on the photoelectric effect. The X-ray beam interacts with an inner shell electron within atoms. If the photons are sufficient, the energies are transferred their entire energy to electrons and electron

received the energy is ejected from the atom becoming a photoelectron. These procedures are shown in Figure 1.4. The photoelectron has a kinetic energy ( $E_k$ ) that determined by the energy of the photon ( $h\nu$ ), the binding energy of the electron ( $E_b$ ). A spectrum consists of a plot of counts of photoelectrons as a function of kinetic energy or binding energy. The  $\phi_{spec}$  in the equation below is work function of the spectrometer.

$$E_b = h\nu - E_k - \phi_{spec}$$

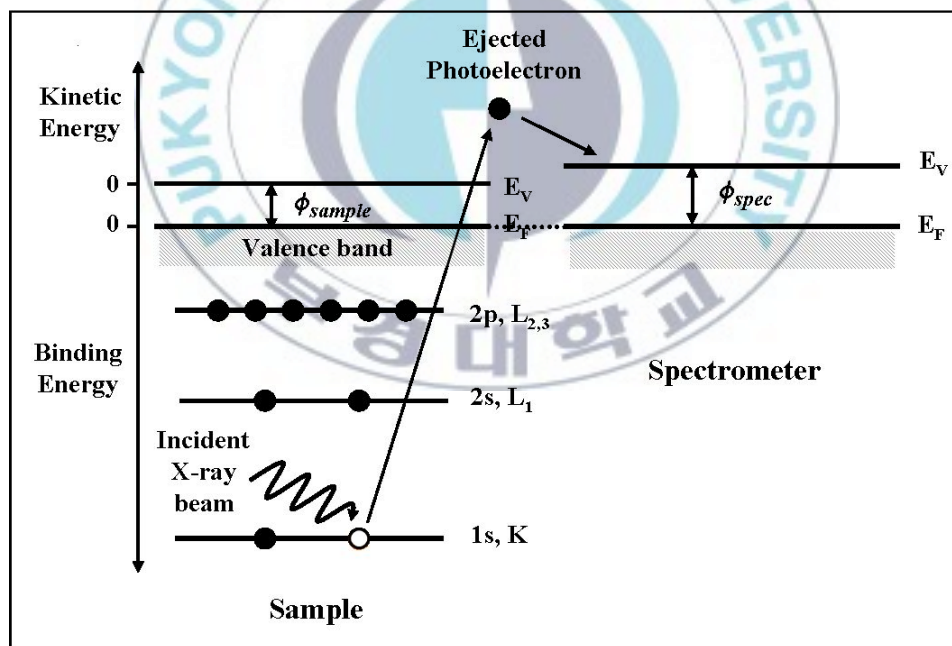


Figure 1.4. Schematic diagram of the XPS process.

Additionally, the Auger electrons can be emitted by electronic relaxation of the atom during the XPS process and the produced Auger electrons will be detected with photoelectrons. The difference between Auger peak and XP spectra is that the Auger peaks are broader than photoemission peak. While the kinetic energy of the Auger electrons is independent of the X-ray energy, the kinetic energy of photoelectrons will be changed by the X-ray source.

When the photoelectron comes from p, d, and f orbitals, two peaks are observed. The separation between the two peaks is based on the spin orbital splitting (SOS) and the value of SOS is different in every element. For any electron around atomic nucleus has the total angular momentum which is obtained by coupling between the orbital angular momenta and spin angular momenta. The two momenta are given the quantum numbers  $l$  and  $s$ , and then the vector sum of those given the quantum number  $j$ . Several atomic and X-ray notations are shown in Table 2. The degeneracy at each  $j$  value is  $2j+1$ , for example, if the shell is p orbital, the values of  $j$  are  $3/2$  and  $1/2$ , then the degeneracy is 4:2, 2:1, and the ratio of peak area is  $2p_{3/2}:2p_{1/2} = 2:1$ .

Table 2. Atomic and X-ray notation.

quantum numbers				Atomic notation	X-ray notation
$n$	$l$	$s$	$j$		
1	0	$\pm 1/2$	$1/2$	$1s_{1/2}$	K
2	0	$\pm 1/2$	$1/2$	$2s_{1/2}$	$L_1$
2	1	$-1/2$	$1/2$	$2p_{1/2}$	$L_2$
2	1	$+1/2$	$3/2$	$2p_{3/2}$	$L_3$
3	0	$\pm 1/2$	$1/2$	$3s_{1/2}$	$M_1$
3	1	$-1/2$	$1/2$	$3p_{1/2}$	$M_2$
3	1	$+1/2$	$3/2$	$3p_{3/2}$	$M_3$
3	2	$-1/2$	$3/2$	$3d_{3/2}$	$M_4$
3	2	$+1/2$	$5/2$	$3d_{5/2}$	$M_5$

One of the most valuable advantages of XPS is its ability to distinguish the elements in the different chemical environment. Different types of chemical bonds affect the binding energy of electrons in an atom. If the charge is transferred from surrounding atom to the specific atom as a result of chemical bond formation, the energy level of both atoms are changed [5-7]. Therefore, comparing data of an unknown sample to those of reference elements leads to the information about identification of the formal oxidation state of the atom and functional group in the sample.

XPS can be also used to quantitative analysis of elements in the sample. The area under a characteristic peak is related directly to the concentration of the corresponding atomic species in the surface layer.

## 1.4. References

- [1] R. Nix (2003), *An Introduction to Surface Chemistry [online]*, available at:  
URL: <http://www.chem.qmw.ac.uk/surfaces/scc/> (Accessed 29<sup>th</sup> November 2005).
- [2] S.J. Garrett, D.V. Heyd, J.C. Polanyi, *J. Chem. Phys.* 106 (1997) 7834.
- [3] K. Nagai, *Phys. Rev. Lett.* 54 (1985) 2159.
- [4] L.A. Harris, *J. Appl. Phys.* 39 (1968) 1419.
- [5] L. Qiu, F. Liu, L. Zhao, W. Yang, J. Yao, *Langmuir* 22 (2006) 4480.
- [6] J. Klinowski, T.L. Barr, *Acc. Chem. Res.* 32 (1999) 633.
- [7] P.K. Babu, A. Lewera, J.H. Chung, R. Hunger, W. Jaegermann, N. Alonso-Vante, A. Wieckowski, E. Oldfield, *J. Am. Chem. Soc.* 129 (2007) 15140.



## CHAPTER 2. Behavior of C<sub>2</sub>D<sub>5</sub>OD on Zircaloy-4 Surfaces

### 2.1. Introduction

Zirconium is classified as a very reactive metal which has a great affinity for oxygen. When zirconium is exposed to an oxygen, a chemically and mechanically protective oxide film is formed. It gives excellent corrosion resistance property used in a variety of applications. And zirconium exhibits a high melting point, good thermal conductivity, low thermal expansion, and a very low thermal neutron scattering cross-section compared with other metals [1]. As a result of these properties, zirconium and its alloys are extensively used as a fuel cladding material and for coolant channels in water cooled power reactors.

Commercially available grades of zirconium alloys are divided to nuclear and chemical grades [2]. Zircaloy-4 (Zry-4) in the nuclear grades was used for this study has compositions of 98.17 wt.% Zr, 1.4 wt.% Sn, 0.23 wt.% Fe, and 0.2 wt.% Cr. Zry-4 has been of great concern and the number of articles deal with a variety of surfaces in many fields, such as corrosion [3-5], oxidation [6-10], and hydrogen absorption [11-14]. Few papers about interaction of adsorbed molecules with Zry-4 have been published [15-17]. Ramsier's group reported about H<sub>2</sub>O adsorption on Zry-4 surfaces at 150 K using AES and TPD methods [18]. They observed surface oxidation through the AES experiment and zeroth-order kinetics is observed in the heating of H<sub>2</sub>O/Zry-4,

but no significant desorption of hydrogen is detected. However, the hydrogen desorption is observed after water adsorption on Zr(0001) [19,20] and oxygen adsorption on polycrystalline zirconium [21].

Ethanol is recently considered as a source of molecular hydrogen for power fuel cells [22-24]. It is attractive because of its renewable nature since it can be manufactured, in high yield by fermentation of crops and contribute to the reduction of global greenhouse gas emissions [25] and air pollution. Although the reaction mechanism of methanol over the zirconium surface have been studied [26-28], the surface chemistry of ethanol dosed on Zry-4 surface is not well known yet. In this chapter, the results of the thermal effect on the surface chemistry of C<sub>2</sub>D<sub>5</sub>OD dosed Zry-4 surface using TPD and AES techniques are presented.

## 2.2. Experimental Section

All experiments were carried out in a stainless-steel UHV chamber at the base pressure of low  $10^{-10}$  Torr. The UHV chamber equipped with a 4-grid retarding field low-energy electron diffraction (LEED) which is combined with a Auger electron spectroscopy (AES) for determination of the chemical composition on the surface and a quadrupole mass spectrometer (QMS) for performing TPD measurements. An Ar ion sputtering gun (IES 5, Omicron) is used for removal of impurities such as carbon and oxygen on the surface before performing TPD experiment. The pumping system consists of a

roughing pump (RP), a turbomolecular pump (TMP), an ion pump (IP), and a Ti-sublimation pump (TSP). The RP used makes the chamber from atmospheric pressure to a low vacuum to allow the high vacuum pump, like a TMP, to operate. The IP and TSP were used to make the ultra high vacuum (UHV). The RP and TMP, except one IP, are separated from the main chamber by gate valves. The pressure was measured with nude ion gauges. In this system, two nude ion gauges were used. One was mounted on the analysis chamber and the other was attached on the preparation chamber.

The Zry-4 sample used in this study has a surface area of  $9.35 \times 9.55 \text{ mm}^2$  and a thickness of 1.70 mm in a rectangular shape. It was prepared through many steps of polishing with different meshes of abrasive papers and mechanical polisher (Buehler, gamma alumina, 0.05 micron) for the final step of surface polishing. Then, the polished Zry-4 was rinsed with acetone in ultrasonic cleaner for ten minutes. After ultrasonic cleaning, the sample was dried with high purity nitrogen gas. The prepared Zry-4 was mounted on the custom designed sample holder by spot welding on Ta wires. The type-K thermocouple was spot welded on the side of the Zry-4 for monitoring sample temperature. Before the experiment was performing, the sample was cleaned by many cycles of Ar ion (99.999% purity, Aldrich) sputtering and annealing to 843 K, then the cleanliness of the Zry-4 surface was checked by AES. During the Ar ion sputtering process, the pressure of  $\text{Ar}^+$  was kept at  $1.5 \times 10^{-5}$  Torr for 1 hour in order to make 20  $\mu\text{A}$  of the target current. And the  $\text{Ar}^+$  fluence was  $5.1 \times 10^{23} \text{ Ar}^+/\text{cm}^2$  per sputtering cycle.

For the reaction of deuterated ethanol ( $C_2D_5OD$ , DE) with Zry-4, the DE (99.5%, at.%) was purified through several times of freeze-pump-thaw (FPT) methods. The DE was chosen to study to differentiate with the residual hydrogen in the UHV chamber. The purity of DE after several cycles of FPT was checked by QMS shown in Figure 2.1. Before introducing the DE into the UHV chamber, the sample was cooled by liquid nitrogen. When the temperature of the sample reached about 190 K, the gas phase DE was backfilled into the chamber with various exposures through a leak valve kept the pressure at  $1.0 \times 10^{-6}$  Torr. After the exposure, the sample was facing to the quadrupole mass spectrometer and linearly heated up to 843 K with heating rate of 1 K/s. The possible desorption species from the DE adsorbed Zry-4 surfaces, such as  $H_2$ , HD,  $D_2$ ,  $H_2O$ ,  $D_2O$ , CO, and  $CD_3O$  were monitored applying multiple ion monitoring (MIM) mode in QMS.

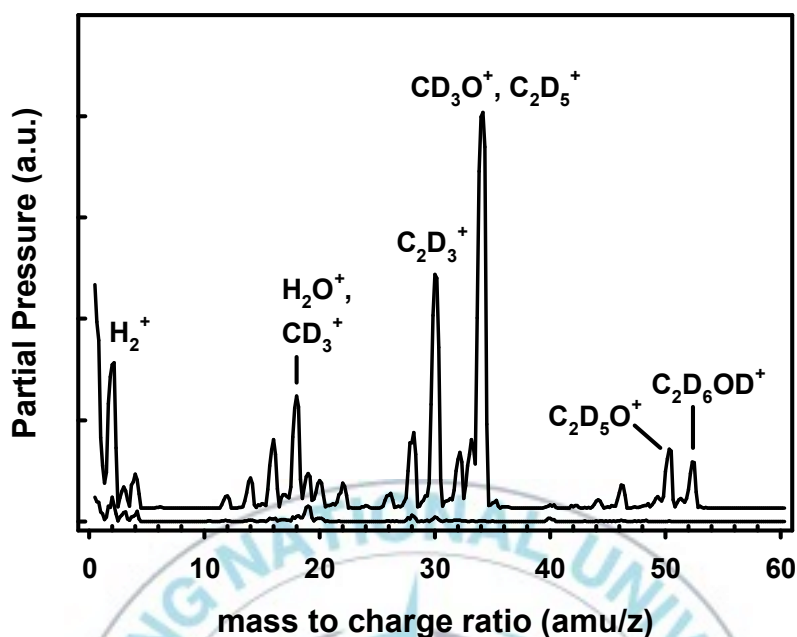


Figure 2.1. Purity of DE checked with the QMS. The bottom line shows the background of the analysis chamber. The top line was taken after purified DE backfilled into the chamber. Even pure deuterized ethanol was used for this work, hydrogen exchange could be occurred in the gas handling system. This caused by  $H_2^+$  peak at 2 amu.

The AES experiments were performed as following procedure. The sample was cooled down about 190 K and exposed to the DE with making desired exposure, then the temperature of sample was increased linearly from 190 K up to certain temperatures (503, 628, 653, 753, and 843 K). Then the sample was cooled down to 190 K and collected the AE spectra for investigation of thermal effect on the DE/Zry-4 system. These temperatures were chosen in according to the results of TPD experiment. When the survey scan of AE spectra was taken with parameters that 3 keV of beam energy, 140  $\mu$ A of beam current, 0.3 mA of emission current, 1.17 A of filament current,

and 75  $\mu$ A of target current. The kinetic energy range for AES applied in this work was from 5 to 600 eV. The data were collected 1 eV of energy step for survey scan, 3 mV of lock-in amplifier. AE spectra were taken at the ranges for zirconium, carbon and oxygen from sensitivity, and 100 ms of lock-in time constant. The high resolution AE spectra of Zr, C, and O were taken from 70 to 180 eV, 240 to 300 eV, and 280 to 540 eV, respectively with 0.2 eV of energy step and other factors were kept the same as applied in the survey scan.

## **2.3. Results and Discussion**

### **2.3.1. Temperature Programmed Desorption: C<sub>2</sub>D<sub>5</sub>OD/Zircaloy-4**

Figures 2.2 (a) and (b) show the representative thermal desorption spectra of 2 amu ( $\text{H}_2^+$  or  $\text{D}^+$ ) and 4 amu ( $\text{D}_2^+$ ), respectively, after different DE exposures at 190 K. The gas exposures were presented by langmuir ( $1 \text{ L} = 1.0 \times 10^{-6} \text{ Torr}\cdot\text{s}$ ) unit. When the exposure of gas was lower than 50 L, no noticeable desorption was observed. Even we used ultra pure deuterized ethanol, hydrogen exchange could be occurred in gas handling line. Because of the hydrogen exchange,  $\text{H}_2^+$  desorption peak was detected. The hydrogen (2 amu) thermal desorption peak was observed at around 660 K at 53 L of ethanol exposure which increased in intensity with rising DE exposure. The desorption peak temperature was shifted to lower temperature according to the increase of gas exposure. This phenomenon could be explained by the second-

order desorption kinetics. Especially, note the  $D_2$  evolution (Figure 2 (b)), the desorption peaks appeared both  $\sim 520$  and  $\sim 660$  K overlapped with broad desorption background desorbing from  $\sim 300$  to  $750$  K. This broad desorption background implies that complicate desorption kinetics was involving in  $D_2$  desorption. The peak position of low temperature desorption feature ( $\sim 520$  K) was constant with increasing the exposures of adsorbate indicating that the desorption of  $D_2^+$  was the first-order desorption verified by peak-shape analysis. The high temperature desorption feature ( $\sim 660$  K) gradually increased in intensity with exposure and shifted to lower temperature. It could indicate the second-order desorption kinetics.

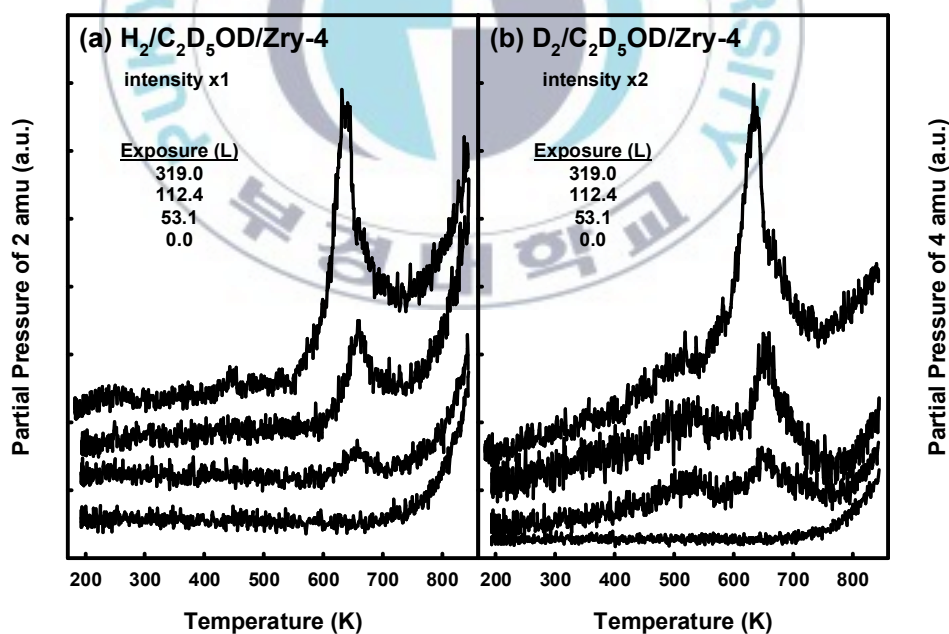


Figure. 2.2. Temperature programmed desorption spectra of (a) 2 amu and (b) 4 amu following DE adsorption on Zircaloy-4 at 190 K. The numbers in the figure represent the exposure in langmuir unit. The notations used in the title of these figures, such as  $H_2/C_2D_5OD/Zry-4$ , means  $H_2$  evolution after DE dosed on the Zry-4 surfaces.

The TPD peaks of 20 amu ( $D_2O^+$ ) and 28 amu ( $CO^+$ ) are shown in Figures 2.3 (a) and (b), respectively. The  $D_2O^+$  and  $CO^+$  desorption temperatures were shifted from around 660 K to lower temperature with increasing exposure of DE. This implies the desorption kinetics of  $D_2O$  and  $CO$  shows the characteristic second-order desorption by peak analysis. However, all of the TPD data ( $H_2^+$ ,  $D_2^+$ ,  $D_2O^+$ , and  $CO^+$ ) did not show symmetric peak shape which is one of the characteristics of the second-order desorption kinetics. These facts infer the desorption kinetics of DE on Zry-4 surfaces is complex rather than one simple first or second-order desorption kinetics. The TPD peak intensity of  $CO^+$  was dramatically increased after the desorption peak maxima shown in Figure 2.3(b). This phenomenon was monitored by measurement of AE intensity of carbon of different annealing temperatures. The results of AES are well agreement with  $CO^+$  TPD data.

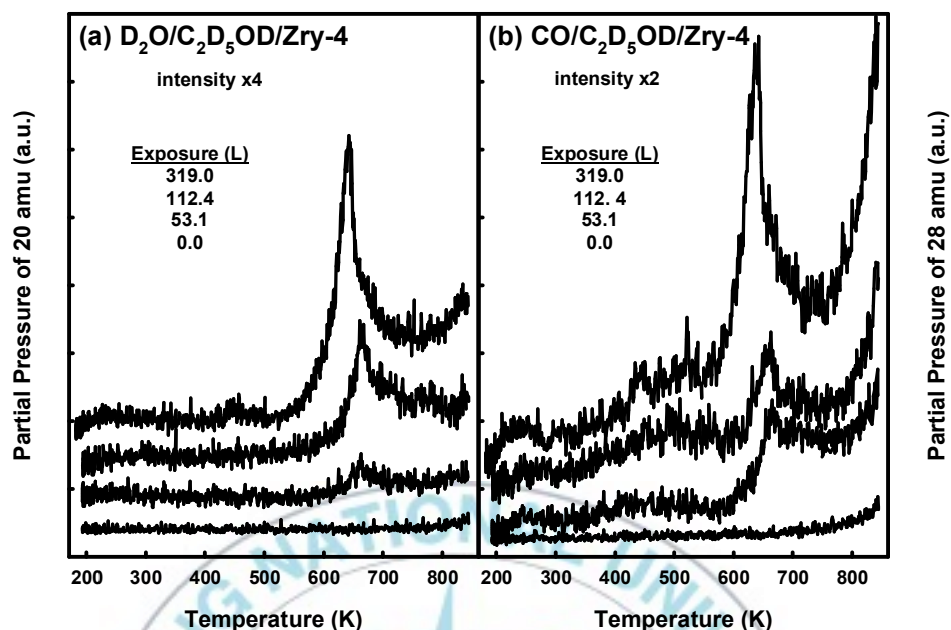


Figure 2.3. Temperature programmed desorption spectra of (a) 20 amu and (b) 28 amu following DE adsorption on Zircaloy-4 at 190 K.

### 2.3.2. Auger Electron Spectroscopy: $C_2D_5OD/Zircaloy-4$

The survey AE spectra of Zry-4 are shown in Figure 2.4. These spectra were taken after stepwise annealing of the sample to our interested temperatures which were chosen considering with the TPD spectra shown in Figures 2 and 3, at and after the desorption peak maximum. The bottom AE spectrum was taken from the clean surface of Zry-4 which was obtained after 10 cycles of  $Ar^+$  sputtering and annealing process. As shown in survey scan of the clean surface of Zry-4, Zry-4 surface contained carbon and oxygen that induced by diffusion from subsurface or bulk of the Zry-4.

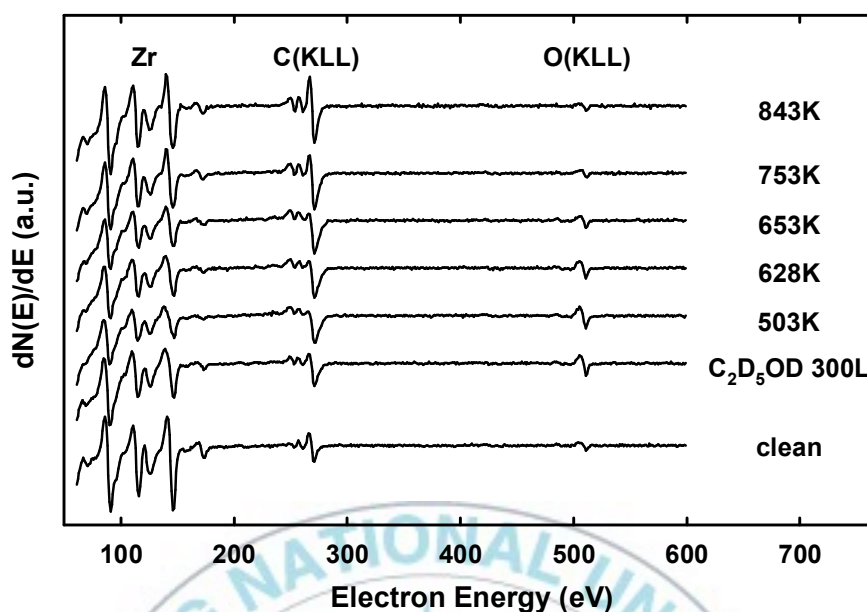


Figure 2.4. Derivative mode of Auger electron spectra of the survey scan of Zircaloy-4.

The high resolution AE spectra of zirconium, carbon, and oxygen atoms are shown in Figures 2.5. According to the theory of producing Auger electrons, Zr features have several types Auger electrons between 70 and 180 eV. Zr(MNV) peak is the most used in analyzing Zr element, because it is the most sensitive about the surface condition (i.e. adsorbed species change the peak shape and/or intensity). The peak intensity of Zr(MNV)<sub>m</sub> (metallic) was decreased after 300 L of DE exposure as we expected and gradually increased by annealing. We should notice in Figure 2.5 (a) that the AE spectra of Zr(MNV)<sub>o</sub> (oxide) is arised following by DE dosing then decreased with increasing the temperature of annealing. This indicates that the oxidation state of zirconium changed from metallic zirconium to zirconium oxide then back to

nearly metallic zirconium by annealing. The change of zirconium oxidation state was supported by the AE spectra of oxygen (Figure 2.5 (b)) as well. The intensity of Zr(MVV) transition involving two valence electrons is also decreased after 300 L of DE exposure and then increased for 753 K. The Zr(MNN) peak was much less changed than other two transitions in terms of low intensity and peak shift [29]. It is evident that the valence band of Zr atoms is easily effected by oxidation state of Zr [30] and then the difference of peak shape and intensity between metallic and oxidized form is more clearly distinguished in Zr(MNV) than Zr(MNN).

The peak positions of C(KLL) and O(KLL) are assigned at the electron kinetic energy of 270 and 510 eV, respectively. As we can see in Figure 2.5 (b), the O(KLL) peak intensity was increased by 300 L of DE exposure. Then the intensity of O(KLL) was decreased by annealing to almost the level before dosing of DE. The peak intensity of C(KLL) were stayed almost constant until the sample temperature of 628 K shown in Figure 2.5 (c). After this temperature C(KLL) intensity was increased by annealing. This is consistent with CO<sup>+</sup> TPD data shown in Figure 2.3 (b). This could be happened that the defragmented carbon in subsurface region was diffused out after the constituents near the surface were desorbed out to vacuum by annealing. These diffused carbon from the subsurface region was not cleaned unless 10 cycles of Ar sputtering process applied.

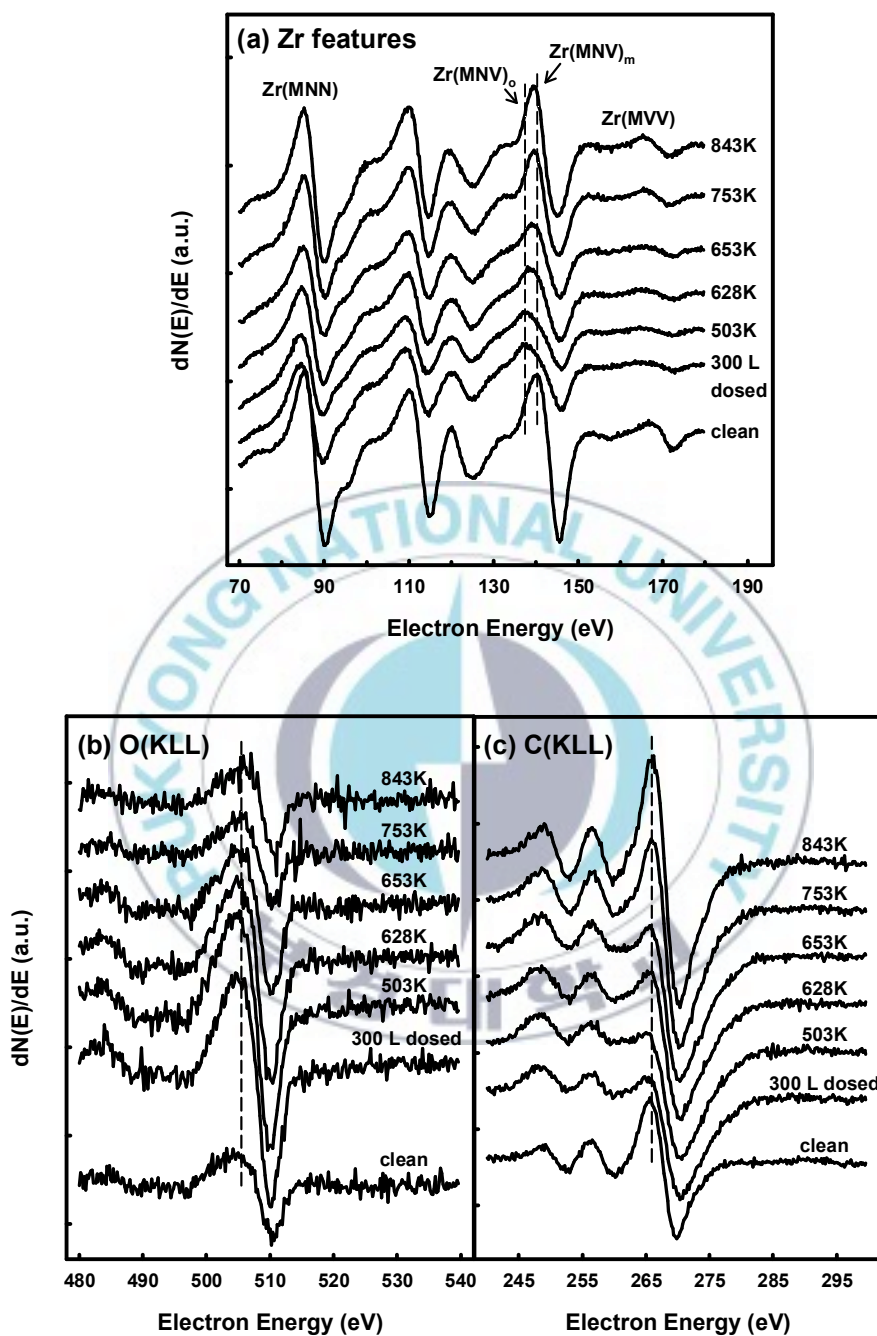


Figure 2.5. (a) Auger electron spectra of the Zr features including Zr(MNN), Zr(MNV)<sub>o</sub>, Zr(MNV)<sub>m</sub>, and Zr(MVV), (b) AES of the C(KLL, 270 eV) peak, and (c) AES spectra of the O(KLL, 510 eV). The vertical lines in the figures were added for clarity.

Figure 2.6 shows the Auger peak-to-peak height (APPH) ratios of C(KLL, 270 eV)/Zr((MNV)<sub>m</sub>, 147 eV) and O(KLL, 510 eV)/Zr(MNV)<sub>m</sub>. The APPH ratios of C/Zr and O/Zr were 1.91 and 0.62, respectively, of the clean surface. The APPH ratios were calculated concerning with Auger sensitivity factors of the elements. The both ratios were increased after 300 L of deuterized ethanol dosing and nearly stayed in constant level until the sample was heated to 628 K. When the sample was heated over 653 K, the ratio of C/Zr was increased gradually but that of O/Zr was decreased nearly back to the clean surface level. The contents of carbon and oxygen on the Zry-4 surface after 600 K were increased by following desorption of D<sub>2</sub>O and CO shown in Figure 2.3 (a) and (b). The carbon diffused onto the surface region by heating formed carbide form with zirconium. The diffused out surface oxygen with large diffusion coefficient could be diffused into the bulk caused relatively lower surface contents of oxygen than that of carbon. These phenomena are consistent with the observation reported by other group [29,31]. The line shape of C(KLL) shown in Figure 2.5(c) should be noticed. The oscillation of peak at low kinetic energy region could be differentiate carbidic and graphitic carbon reported by Gomer's group [32]. The peak oscillation of low kinetic energy region of C(KLL) was diminished when the sample was annealed to 503 K, then the oscillation was recovered with further annealing the sample to 843 K. This implies that the dominant carbon state of DE/Zry-4 changed from carbidic to graphitic through to carbidic carbon on the surface by annealing.

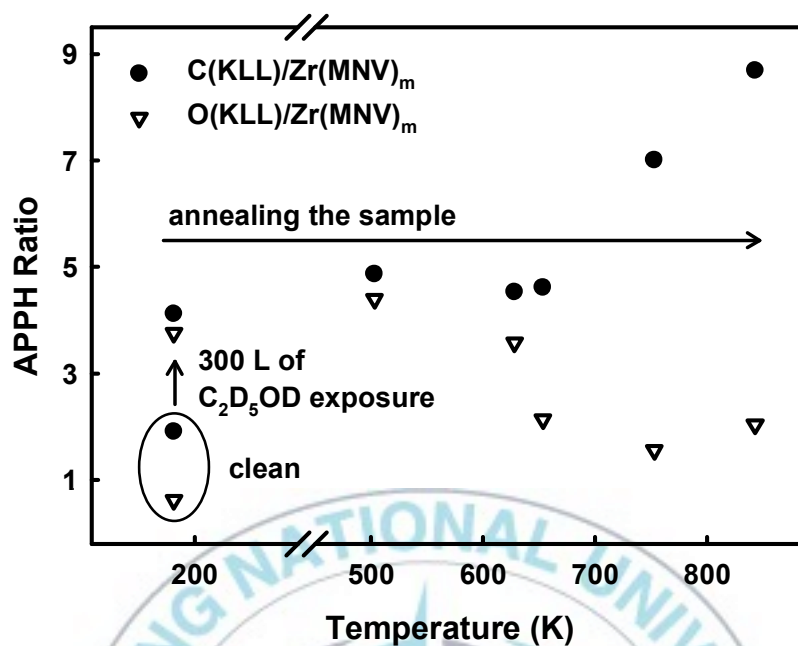


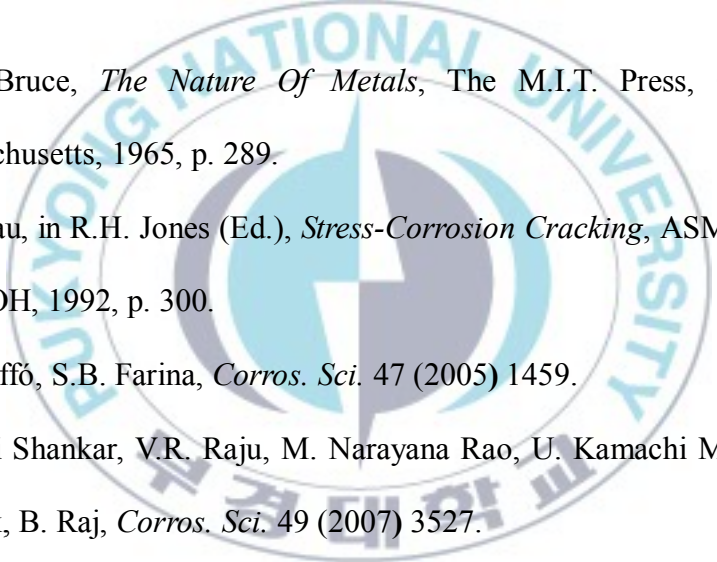
Figure 2.6. Auger peak-to-peak heights (APPH) ratio versus annealing temperature. Filled circles represent for  $C(KLL)/Zr(MNV)_m$  and hollow triangles represent for  $O(KLL)/Zr(MNV)_m$ . The data inside of the circle bottom of the left in the figure present APPH ratios of C/Zr and O/Zr of the clean Zry-4 surface.

## 2.4. Conclusion

The surface chemistry of  $C_2D_5OD$  on Zry-4 surface was investigated using AES and TPD methods. Isotopic hydrogen was detected from deuterized ethanol dosed Zry-4 surfaces at two different desorption temperature regions accompanying with broad desorption background. This shows the possibility of using hydrocarbon derivatives for the source of hydrogen used in a fuel cell. The lower temperature feature at around 520 K stayed at the same temperature increasing  $C_2D_5OD$  exposure. This implies  $D_2$  desorption is first-order

desorption kinetics. The TPD peak of D<sub>2</sub> at around 650 K was shifted to lower desorption temperature as the exposure of C<sub>2</sub>D<sub>5</sub>OD increased. In AES study revealed that the metallic zirconium was oxidized by deuterized ethanol adsorption then reduced back to metallic zirconium by annealing because the oxygen near the surface was depopulated by heat treatment.

## 2.5. References

- 
- [1] A.R. Bruce, *The Nature Of Metals*, The M.I.T. Press, Cambridge, Massachusetts, 1965, p. 289.
- [2] T.-L. Yau, in R.H. Jones (Ed.), *Stress-Corrosion Cracking*, ASM, Materials Park, OH, 1992, p. 300.
- [3] G.S. Duffó, S.B. Farina, *Corros. Sci.* 47 (2005) 1459.
- [4] A. Ravi Shankar, V.R. Raju, M. Narayana Rao, U. Kamachi Mudali, H.S. Khatak, B. Raj, *Corros. Sci.* 49 (2007) 3527.
- [5] M.Y. Yao, B.X. Zhou, Q. Li, W.Q. Liu, X. Geng, Y.P. Lu, *J. Nucl. Mater.* 374 (2008) 197.
- [6] P.B. Bozzano, M. Ipohorski, R.A. Versaci, *Acta Microscópica*, 13 (2004) 47.
- [7] S. Abolhassani, M. Dadras, M. Leboeuf, D. Gavillet, *J. Nucl. Mater.* 321 (2003) 70.
- [8] Y.S. Park, Y.K. Ha, S.H. Han, K.Y. Jee, W.H. Kim, *J. Nucl. Mater.* 372 (2008) 59.

- [9] G. Moulin, R.E. Tahhan, J. Favergeon, M. Viennot, P. Berger, *Mater. Sci. Forum.* 522-523 (2006) 425.
- [10] N. Stojilovic, R.D. Ramsier, *J. Nucl. Mater.* 350 (2006) 163.
- [11] M. Steinbrück, *J. Nucl. Mater.* 334 (2004) 58.
- [12] B.H. Lim, H.S. Hong, K.S. Lee, *J. Nucl. Mater.* 312 (2003) 134.
- [13] M.P. Gómez, G. Domizzi, M.I. López Pumarega, J.E. Ruzzante, *J. Nucl. Mater.* 353 (2006) 167.
- [14] S. Yamanaka, K. Higuchi, K. Miyake, *J. Alloys. Compd.* 231 (1995) 503.
- [15] N. Stojilovic, N. Farkas, R.D. Ramsier, *Appl. Surf. Sci.* 254 (2008) 2866.
- [16] N. Stojilovic, R.D. Ramsier, *J. Vac. Sci. Technol. A* 24 (2006) L7.
- [17] H.Y. Jung, Y.C. Kang, *Bull. Korean Chem. Soc.* 28 (2007) 1751.
- [18] N. Stojilovic, ; R D. Ramsier, *Appl. Surf. Sci.* 252 (2006) 5839.
- [19] B. Li, K. Griffiths, C.-S. Zhang, P.R. Norton, *Surf. Sci.* 384 (1997) 70.
- [20] B. Li, K. Griffiths. C.-S. Zhang, P.R. Norton, *Surf. Sci.* 370 (1997) 97.
- [21] W.J. Peterson, R.E. Gilbert, *Appl. Surf. Sci.* 24 (1985) 121.
- [22] P.-Y. Sheng, A. Yee, G.A. Bowmaker, H. Idriss, *J. Catal.* 208 (2002) 393.
- [23] A.M. Silva, L.O.O. Costa, A.P.M.G. Barandas, L.E.P. Borges, L.V. Mattos, F.B. Noronha, *Catal. Today* 133 (2008) 755.
- [24] A.M. Silva, A.P.M.G. Barandas, L.O.O. Costa, L.E.P. Borges, L.V. Mattos, F.B. Noronha, *Catal. Today* 129 (2007) 297.
- [25] V.A. Goltsov, T.N. Verziroglu, *Int. J. Hydrogen Energy* 26 (2001) 909.
- [26] N. Stojilovic, D.W. Weber, R.D. Ramsier, *Appl. Surf. Sci.* 218 (2003) 188.
- [27] N. Stojilovic, R.D. Ramsier, *J. Vac. Sci. Technol. A* 22 (2004) 1631.

- [28] J.L. Bronkema, A.T. Bell, *J. Phys. Chem. C* 112 (2008) 6404.
- [29] N. Stojilovic, N. Farkas, R.D. Ramsier, *Appl. Surf. Sci.* 254 (2008) 2866.
- [30] C. Zhang, P.R. Norton, *J. Nucl. Mater.* 300 (2002) 7.
- [31] N. Stojilovic, D.W. Weber, R.D. Ramsier, *Appl. Surf. Sci.* 218 (2003) 188.
- [32] J.E. Whitten, R. Gomer, *Surf. Sci.* 347 (1996) 280.



## **CHAPTER 3. Characterization of Nanofibers Synthesized by Electrospinning**

### **3.1. Characterization of Titania Doped Nanofibers**

#### **3.1.1. Introduction**

Nanostructured metal oxides have attracted significant attention due to its physical and chemical properties and potential applications in many areas such as catalysis, electronic, and photoelectronic devices. Recently, titanium oxide (titania,  $\text{TiO}_2$ ) is considered as one of the most important ceramic materials used in practical applications in photovoltaic cells [1], photocatalysts [2], and gas sensors [3]. The  $\text{TiO}_2$  has three different crystal structures those are brookite, anatase, and rutile [4]. The rutile phase has the highest refractive index and ultraviolet absorption cross-section, thus it has wide applications in paints [5], cosmetics [6], and ultraviolet absorbents [7]. Generally, the anatase phase has a chemically and optically higher activity than rutile, it is suitable for catalysts [8] and catalytic supports [9]. Because of the different characteristics between anatase and rutile, the behavior which is transformed from anatase to rutile have been studied in various synthesis conditions [10,11].

Various methods to produce nano- and micro-structures of titania have been reported, such as sol-gel processes [12], chemical vapor deposition [13], vapor phase pyrolysis [14] or hydrolysis [15], and electrospinning [16].

In this research, titania nanofibers were fabricated by dip-coating electrospun polymeric fibers into sol-gel precursors. During post-coating annealing, the titania nanofibers have two different forms, anatase or rutile, depending on the temperature, as verified by several different techniques. Most importantly, based upon results from X-ray photoelectron spectroscopy (XPS) we compare the electronic structure of the two phases of titania coated nanofibers to demonstrate that our synthesis methods could be used to produce nanofibers with different physical properties which could therefore be tailored for specific applications.

### **3.1.2. Experimental Section**

Titania nanofibers were prepared by sol-gel coating of a template made from electrospun nylon nanofibers. Nylon-6 (Aldrich, MW. 4,322) was dissolved in formic acid (Fisher Scientific) at a 20:80 wt.% ratio. This solution was electrospun into nanofiber mats using a laboratory-scale electrospinning apparatus [17]. The polymer mixture was loaded into a 5 ml plastic syringe with a flexible silicone tube at one end and a 21 gauge stainless steel needle at the other end. The needle was connected to a high voltage supply (Gamma High Voltage Research Inc. Ormond Beach, FL) operated at 20 kV DC. The feeding rate for the Nylon-6 solution was controlled using a syringe pump

(World Precision Instruments, Sarasota, FL; SP1011) at 2.0  $\mu\text{l}/\text{min}$  with the needle positioned about 15 cm above the grounded collector. The collector was aluminum foil wrapped around a 12.5 cm diameter cylindrical wire drum. The drum was rotated on its axis at a rate of about 1 revolution per minute.

In order to deposit titania on the surface of the Nylon-6 nanofibers, the fiber mats were submerged into a sol-gel solution which consisted of 144 ml distilled water, 20 ml of 5 M nitric acid (Fisher Scientific), 10 ml of isopropyl alcohol (Fisher Scientific), and 2 ml of titanium isopropoxide (Aldrich). In order to make the anatase form of titania, the submerged nanofiber mat was heated from 60°C to 95°C at a rate of 5°C/min and held at 95°C for about 90 minutes until the solution turned to a milky white color. To make the rutile form, the coated nylon nanofibers were heated from room temperature to 60°C at a rate of 0.5°C/min and held at 60°C for 3 to 4 hrs until the solution became milky. This heating induced the growth of titania nanoparticles on the surfaces of the fibers. The titania-coated nanofibers were removed from the sol solution and washed several times with methanol to remove any residual alkoxides. The nanofibers were then heated to 350°C to form anatase titania and 700°C to form rutile titania.

The morphology of the aforementioned titania fibers was observed by scanning electron microscopy (SEM; JEOL Ltd., JSM 5310, Tokyo, Japan). The vibrational spectra were acquired using diffuse reflectance Fourier transform infrared spectroscopy (DRIFTS; Bruker Optics, IFS 66v/S, Tucson, AZ). The crystalline phase of the titania fibers was identified by wide angle X-

ray diffraction (WAXD; Rigaku Co., Ltd., Tokyo, Japan) in the reflection mode with Cu K $\alpha$  radiation.

The chemical nature of the titania nanofibers was investigated with X-ray photoelectron spectroscopy (XPS; VG ESCALAB MK II, West Sussex, UK). The base pressure in the analysis chamber was less than  $7.6 \times 10^{-10}$  Torr. The XPS system was equipped with a twin anode X-ray source, Mg K $\alpha$  (1253.6 eV) and Al K $\alpha$  (1486.6 eV), and a concentric hemispherical analyzer (CHA). During all experiments discussed here, spectra were obtained using the Al K $\alpha$  X-ray source. The parameters used for XPS experiments were an anode voltage of 9 kV, an electron multiplier voltage of 2850 eV, anode current of 20 mA, filament current of 4.2 A, pass energy of 50 eV, dwell time of 100 ms, and energy step size of 0.5 eV in constant analyzer energy (CAE) mode for survey scans. High resolution scans were performed at an energy step size of 0.02 eV and a pass energy of 20 eV with all other parameters the same as used in the survey scans. XPS data were collected from several different samples and all exhibited similar trends and reproducibility. In each binding energy region, spectra were signal averaged up to 15 times in order to improve the signal to noise ratios. The schematic diagram of XPS apparatus is shown in Figure 3.1.

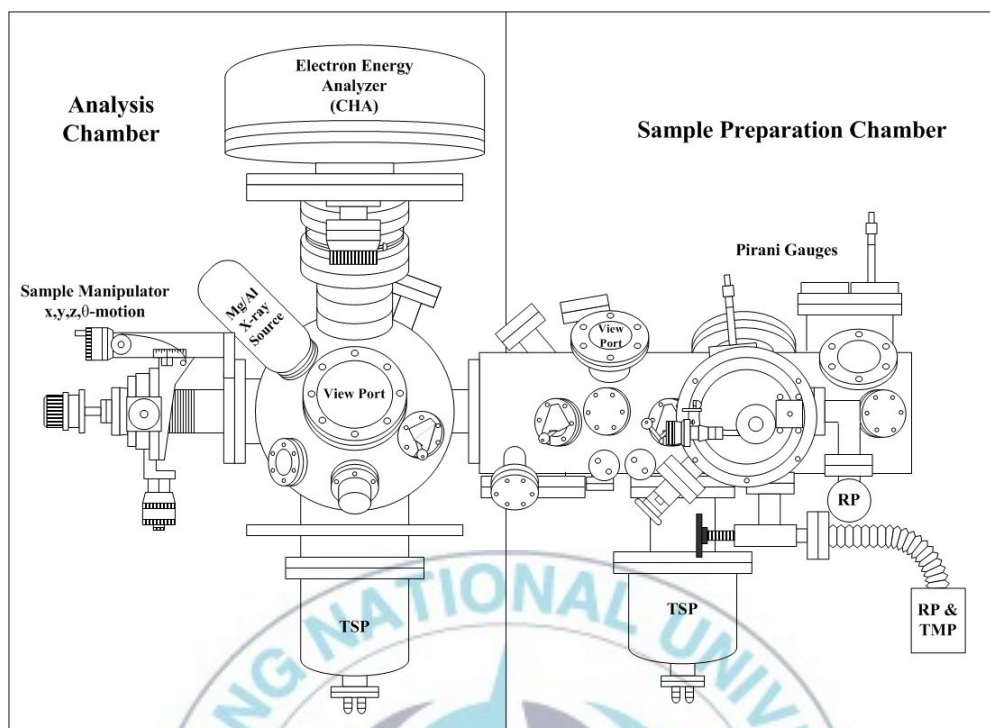


Figure 3.1. The schematic diagram of XPS chamber (VG ESCALAB MK II).

### 3.1.3. Results and Discussion

The morphology and diameter of sol-gel coated titania nanofibers were investigated by SEM, as shown in Figure 3.2. Titania particles were formed during the sol-gel process which precipitated and attached themselves to the polymer nanofibers. The average diameter of the titania particle-coated Nylon-6 fibers is about 250 nm after heating to 120°C (Figure 3.2 (a)) and about 200 nm after heating to 350°C (Figure 3.2 (b)). Rutile titania nanofibers exhibited similar diameters after heating to 700°C. The decreasing diameter of fibers at

higher temperature is due to the removal of solvent and hydrocarbons and the decomposition of the nylon fibers.

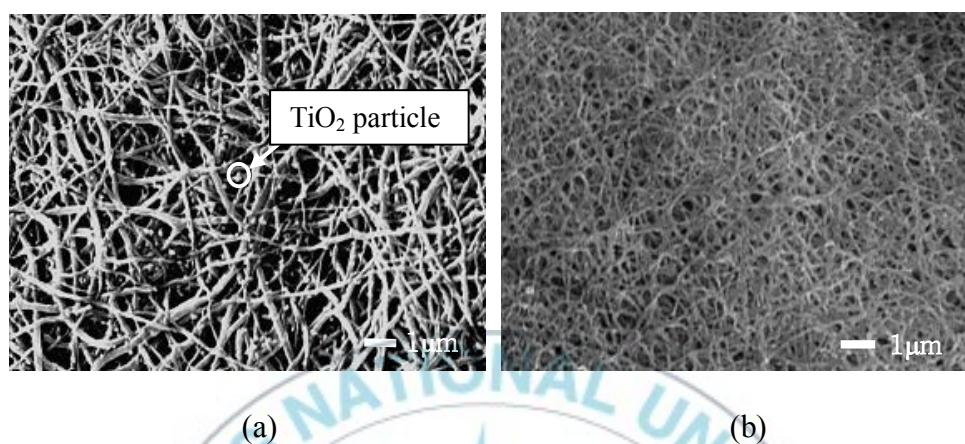


Figure 3.2. Scanning electron microscopy (SEM) images of, (a) titania sol-coated nylon fibers calcined at 120 °C, and (b) calcined at 350 °C.

In order to identify the chemical nature of the synthesized nanofibers, DRIFT measurements were carried out yielding spectra as shown in Figure 3.3. The characteristic vibrational bands in sol-gel coated Nylon-6 nanofibers appeared in the range of 3500-3300 and 1650-1580  $\text{cm}^{-1}$  for N-H stretching and bending modes, 2960-2850 and 1470-1350  $\text{cm}^{-1}$  for C-H stretching, scissoring and bending, 1760-1670  $\text{cm}^{-1}$  for the C-O stretching bands, and 1340-1020  $\text{cm}^{-1}$  for the C-N stretching band. The coated fibers, after heating to 120 and 275°C, still have significant IR absorption features corresponding to vibrations of Nylon-6. Figure 3.3 (c), shows that Ti-O vibrations dominate around 900  $\text{cm}^{-1}$ , indicating that pyrolysis of the nylon has occurred after calcining to 350°C and the anatase titania phase has formed. Also, the

formation of a sequestered form of carbon dioxide is evidenced by the feature around  $2340\text{ cm}^{-1}$  [18]. The absorption bands at  $1636$  and  $3000\text{ cm}^{-1}$  in these spectra indicate the presence of hydroxyl groups. Rutile titania nanofibers (Figure 3.3 (d)) exhibited DRIFT spectra very similar to those from the anatase form.

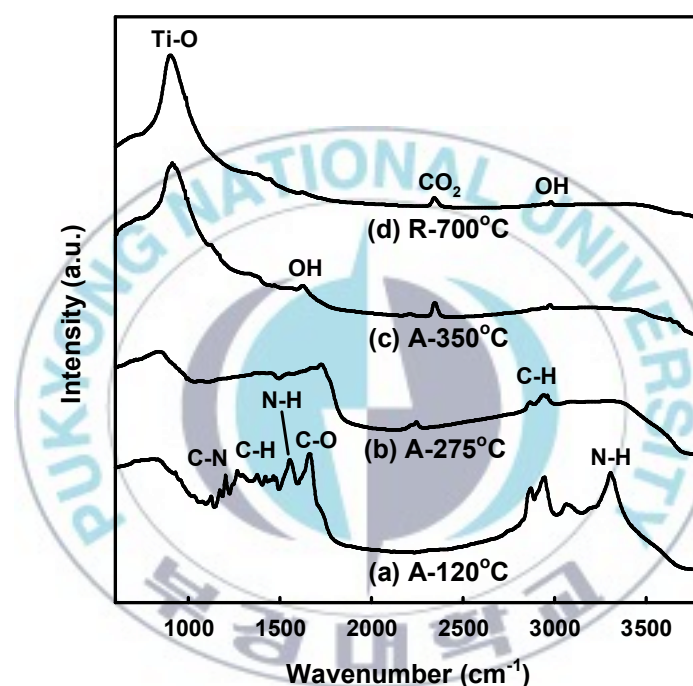


Figure 3.3. DRIFT spectra from titania-coated Nylon-6 nanofiber mats after heating to (a) anatase- $120^{\circ}\text{C}$ , (b) anatase- $270^{\circ}\text{C}$ , (c) anatase- $350^{\circ}\text{C}$ , and (d) rutile- $700^{\circ}\text{C}$  (A = anatase and R = rutile).

Wide angle X-ray diffraction was used to identify the crystal structures of the nanofibers, as illustrated in Figure 3.4. When the heating rate was fast ( $5^{\circ}\text{C}/\text{min}$ ), anatase titania was formed after calcination at  $350^{\circ}\text{C}$  (Figure 3.4 (a)). It was found that all the sharp features observed at  $2\theta = 25.39, 38.11, 48.47, 54.5, 55.01, 62.5,$  and  $68.5^{\circ}$  in the XRD pattern are assigned to anatase

(101), (004), (105), (200), (211), (204) and (116), respectively. The lattice constants determined for the anatase nanofibers are  $a = 0.3772$  nm and  $c = 0.9505$  nm. On the other hand, when the solution was slowly heated ( $0.5^\circ\text{C}/\text{min}$ ) and calcinated at  $700^\circ\text{C}$ , rutile titania resulted (Figure 3.4 (b)). The (110), (101), (220), (111), (211), (220), (002), (310) and (301) features can be indexed to the rutile titania crystal structure with lattice parameters  $a = 0.4566$  nm and  $c = 0.295$  nm [19]. Depending on the heating rate and calcining temperature the crystal structures of the nanofibers could therefore be manipulated to yield distinct properties from the same starting materials [20].

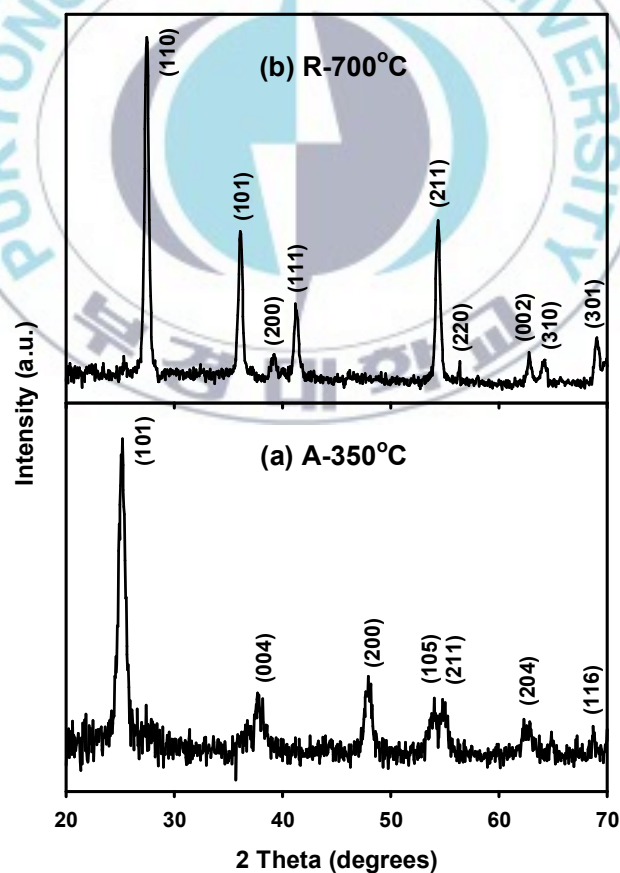


Figure 3.4. XRD spectra for (a) anatase titania nanofibers calcined at  $350^\circ\text{C}$  and (b) rutile titania fibers calcined at  $700^\circ\text{C}$

High resolution XPS data from the Ti 2p and valence band regions comparing rutile and anatase titania are shown in Figures 3.5 (a) and (b), respectively. As seen in Figure 3.4 (a), the doublet peaks of Ti 2p were observed at 459 (Ti 2p<sub>3/2</sub>) and 465 eV (Ti 2p<sub>1/2</sub>) in both rutile and anatase titania. These are the characteristic Ti 2p XPS features of titania. The similar peak positions for both forms of nanofibers imply that the core level binding energy of Ti on the surface does not depend significantly on the crystal structure. However, the electronic structure of the valence band region was affected by structure as shown in Figure 3.5 (b). This structure dependence on the valence band observed in this work has also been identified by Rossi's group in their investigation of a nickel-based alloy using XPS [21]. They identified that the binding energies of Ni core levels, such as Ni 2p<sub>3/2</sub> and Ni 2p<sub>1/2</sub>, were not affected by different crystal structures, but the valence level (the Ni 3d region in their case) was altered by changes in phase.

In Figure 3.5 (b), the top two curves represent XPS data from rutile and anatase titania and the bottom trace shows the spectral intensity obtained by subtraction of the XPS intensity of rutile titania from that of anatase. It is clear that the band structure ca. 3 eV below the Fermi level shows positive peak intensity. This means that anatase titania exhibits a higher density of states than rutile and that anatase has less covalent bond character. This is consistent with the rutile phase having the higher thermodynamic stability [20].

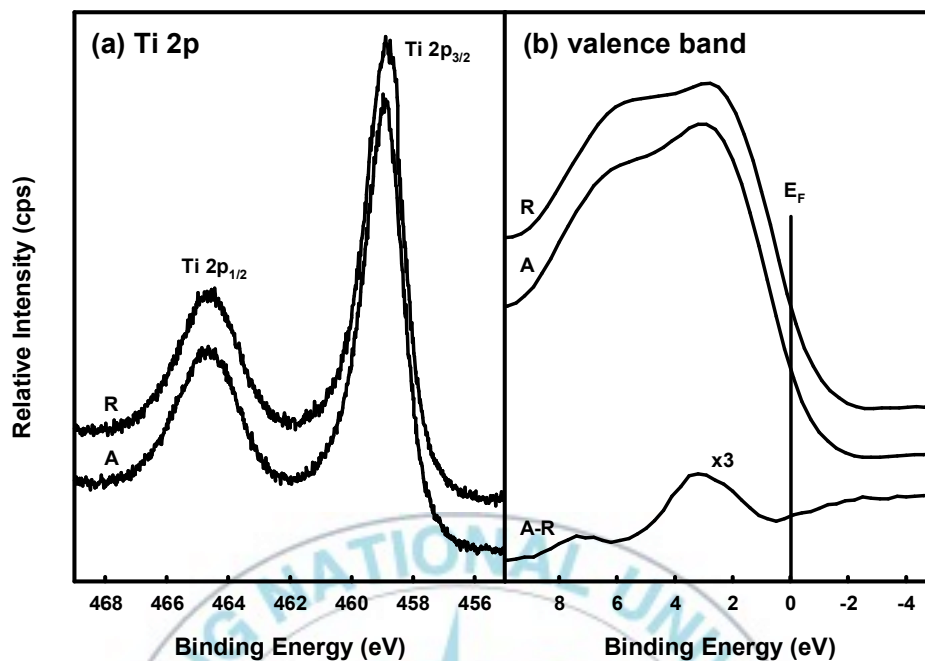


Figure 3.5. High resolution XPS spectra of the Ti 2p region (a) and valence band region (b) comparing rutile and anatase titania (A = anatase, R = rutile, A-R = subtraction of rutile XPS intensity from anatase XPS intensity).

### 3.1.4. Conclusion

Titania nanofibers with average diameters of 200 nm were synthesized by sol-gel coating of electrospun nylon nanofibers followed by calcination. The XRD results show that the crystalline phases were either anatase or rutile forms of titania depending on the heating method. Photoelectron emission data demonstrate that while the crystal structures of titania affected the electronic structure of the valence band region, it did not affect the core level structure, such as Ti 2p<sub>3/2</sub> and Ti 2p<sub>1/2</sub>.

## **3.2. Structural, Electrical, and Optical Properties of Aluminum Oxide Doped Zinc Oxide (AOZO) Nanofibers**

### **3.2.1. Introduction**

Zinc oxide is a well-known wide-band gap wurtzite structured semiconducting oxide material which lies on the border between ionic and covalent semiconductors [22]. Pure and doped zinc oxide nanostructured materials have recently attracted considerable interest due to their unique physical properties and a wide range of possible applications [23-25]. However, pure zinc oxide is not stable in air and its electrical properties are significantly affected by adsorption of O<sub>2</sub>, CO<sub>2</sub>, hydrocarbons, S-containing compounds, and water [26]. Therefore, single crystals and polycrystalline films of zinc oxide have been doped to enhance their mechanical, electrical, and optical properties with elements of the alkali metals such as Li and with Ga, In, N, Al, Sn, P, etc. from groups IIIB to VIIB [26].

One dimensional (1D) alumina doped zinc oxide nanostructures offer a very interesting class of materials for a wide variety of applications in different kinds of devices. Alumina doped zinc oxide has been widely investigated for its application as a transparent conducting oxide in the electric and optoelectronic industries [27]. It has applications as a conducting window material for solar cells [28-31] as well as for active layers of light emitting diodes and laser diodes emitting in the UV spectral region [32]. It is also being

investigated for applications in electrophotography [33], gas sensing [34], and thermoelectric [35]. Undoped and doped zinc oxide films have been usually grown by various deposition techniques, such as pulsed laser deposition [36-38], DC magnetron sputtering [39], RF magnetron sputtering [40,41], metal organic chemical vapor deposition [42], molecular beam epitaxy [43], metal organic vapor phase epitaxy [44], reactive deposition [45], spray pyrolysis [46], and sol-gel [47-50] on different substrates.

In this chapter electrospinning, a simple method to fabricate nanoscale fiber materials, was used to synthesize aluminum oxide doped zinc oxide (AOZO) nanofibers. The average diameter of the fibers was determined to be about 100 nm. Modifications of the crystal structure, optical absorption properties, electrical conductivity and chemical makeup brought about by doping of these nanofibers have been studied. These AOZO nanofibers have potential applications in catalytic, photocatalytic, photonic, electronic, and sensor devices.

### 3.2.2. Experimental Section

AOZO nanofibers were prepared by adding sol-gel precursors to polymer solution and by electrospinning the polymer solution. For the zinc oxide precursor solutions, zinc acetate ( $\text{Zn}(\text{CH}_3\text{COO})_2$ ) was dissolved in water at a mass ratio of 1:4 of  $\text{Zn}(\text{CH}_3\text{COO})_2$  to water. A Polyvinylpyrrolidone (PVP) – ethanol solution of a mass ratio of 1:6 of PVP to ethanol was added to the aqueous zinc acetate solution at a mass ratio of 1:1. The aluminum oxide

precursor solution prepared with a mass ratio of 1:1:1 of aluminum acetate ( $\text{Al}(\text{CH}_3\text{COO})_3$ ) to water to ethanol was magnetically stirred for 24 hrs at room temperature. Another PVP solution, mass ratio of 3:40 of PVP to ethanol, was added to the aluminum acetate solution at a mass ratio of 1.7:1 of PVP to aluminum acetate. The amount of this PVP/ $\text{Al}(\text{CH}_3\text{COO})_3$  composite solution that was added to the PVP/ $\text{Zn}(\text{CH}_3\text{COO})_2$  solution was varied to form the electrospinning solution according to the amount of doping desired. The electrospinning solution was magnetically stirred for 1 hr at room temperature before electrospinning.

The electrospinning solutions were electrospun at 20 kV and constant solution flow rate of 2  $\mu\text{l}/\text{min}$  with a 20 cm distance from the needle tip to the fiber collector. The resultant fibers were heated to 873 K at rate of 10 K/minute and then kept at 873 K for 5 hrs to yield ceramic nanofibers. Compositions and characteristics of four different AOZO samples used in this investigation are summarized in Table 3.

Table 3. Metallic elemental compositions of the four different aluminum oxide doped zinc oxide (AOZO) nanofiber samples after calcining at 873 K for 5 hrs.

Sample	Atomic Ratio in Electrospinning Solution	Average Crystallite Size (nm)
ZnO (Undoped)	0	41.78
AOZO1	0.70	32.16
AOZO2	1.00	36.35
AOZO3	1.35	38.01

For SEM (Hitachi S-2150) analysis, the nanofibers were placed on an aluminum stub with a strip of carbon tape applied to the surface to promote fiber adhesion while minimizing charging effects. The samples were silver-coated (S150B Sputter Coater, Edwards), and imaged using an accelerating voltage of 20 kV. Average fiber diameters were calculated from 50 data points. X-ray powder diffraction patterns were obtained with a Philips diffractometer employing Cu K $\alpha$  radiation, with  $2\theta$  in the range of  $10^\circ$  to  $60^\circ$  to examine the crystalline structures of the AOZO nanofibers. The X-ray source was operated at 40 kV and 35 mA of beam current. A Cary 300 Spectrophotometer was used to obtain the UV-Vis diffusive reflectance spectra of the AOZO nanofibers. Samples were grinded to a fine powder and packed into a shallow stainless steel sample plaque. The optical diffusive reflectances of the samples were measured in the wavelength range of 200-800 nm. In order to investigate the electrical properties of the AOZO nanofibers, I-V measurements were performed using a Keithley 2410 sourcemeter. For these measurements the AOZO nanofibers were grinded and formed into disks (6 mm diameter and 0.75 mm thick) at a hydrostatic pressure of 45 MPa. A thin layer of nickel metal with a thickness of 150 nm was deposited on the flat surfaces of the disk using plasma enhanced physical vapor deposition. Then the nickel coated AOZO disks were placed on an insulating glass slide and electrical contacts were made with silver paste at the two flat surfaces using Ag wires where potential differences of  $\pm 50$  V were applied. X-ray photoelectron spectroscopy (XPS; VG ESCALAB MK II, West Sussex, UK) was used for investigating

the chemical nature of the AOZO nanofibers. The base pressure of the XPS chamber was less than  $1 \times 10^{-9}$  mbar. A twin anode X-ray source with Mg K $\alpha$  (1253.6 eV) and Al K $\alpha$  (1486.6 eV) and a concentric hemispherical analyzer (CHA) were housed in the XPS system. The XP spectra were taken using the Al K $\alpha$  X-ray source. The parameters used for XPS experiments were an anode voltage of 9 kV, an electron multiplier voltage of 2850 eV, an anode current of 20 mA, a filament current of 4.2 A, a pass energy of 20 eV, a dwell time of 100 ms, and an energy step size of 0.02 eV in constant analyzer energy (CAE) mode for high resolution scans.

### **3.2.3. Results and Discussion**

Figure 3.6 shows a representative SEM image of AOZO nanofibers. The average diameter for AOZO nanofibers was determined to be approximately 100 nm. There was no significant change in the average diameters of zinc oxide nanofibers with varying aluminum concentration in the nanofiber matrix.

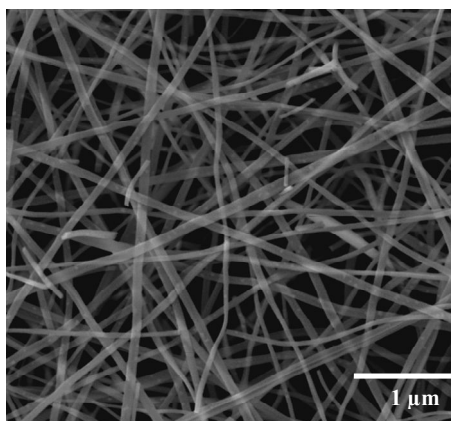


Figure 3.6. Representative SEM image of aluminum oxide doped zinc oxide nanofibers (sample AOZO1) exhibiting an average fiber diameter 100 nm after being calcined at 873 K for 5 hrs.

The diffraction patterns of different AOZO nanofiber samples calcined at 873 K for 5 hrs are presented in Figure 3.7. The XRD patterns indicate that all of the nanofiber structures are well crystallized after calcining at 873 K. The diffraction peaks for the zinc-based materials in Figure 3.7 are consistent with the hexagonal zinc oxide crystal structure reported in literature [51]. The crystallite size  $D$  was calculated from the (101) peak width using Scherrer's formula,

$$D = \frac{K\lambda}{B \cos \theta},$$

where  $D$ ,  $\lambda$ ,  $\theta$ , and  $B$  are the mean crystallite size, the X-ray wavelength, Bragg diffraction angle, and full width half maximum (FWHM) of the diffraction peak of the (101) at around  $36.3^\circ$  for aluminum oxide doped zinc

oxide nanofibers, respectively. No peaks were observed due to alumina in the zinc oxide nanofiber matrix. The micro-structural parameters of the four different nanofiber samples based on the XRD patterns are given in Table 4. The crystallite size and lattice parameters were found to decrease with the addition of aluminum oxide dopant (AOZO1) compared to undoped zinc oxide nanofibers (Figure 3.8). These results indicate the substitution of Zn atom (atomic radius,  $r_{\text{Zn}}$  is 0.74 Å) by smaller Al atom ( $r_{\text{Al}}$  is 0.535 Å) into the ZnO lattice. Further increase of dopants again increases the crystallite size. It indicates possible segregation of Al,  $\text{Al}^{3+}$ , or  $\text{Al}_2\text{O}_3$  at the grain boundaries.

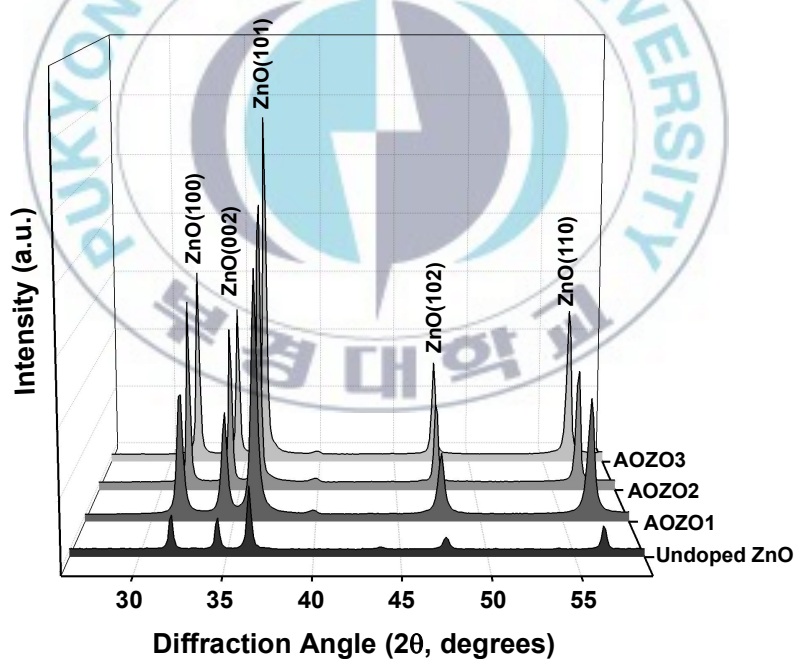


Figure 3.7. XRD patterns of undoped and aluminum oxide doped zinc oxide nanofibers calcined at 873 K for 5 hrs.

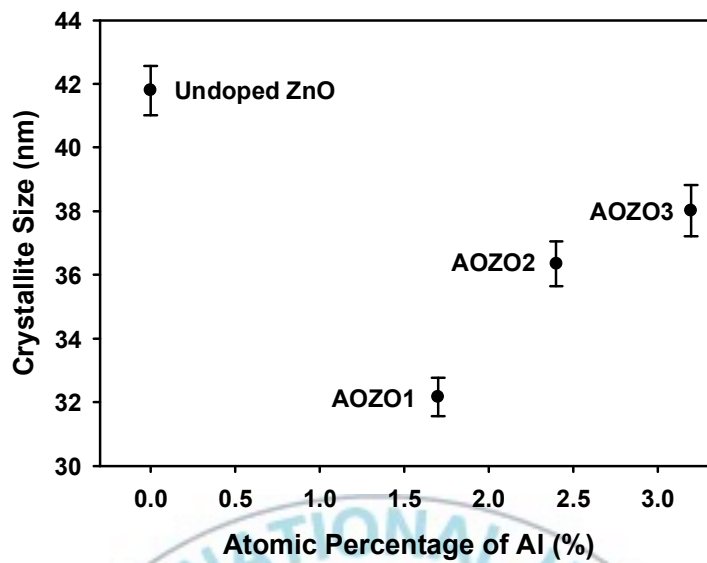


Figure 3.8. Crystallite size of zinc oxide nanofibers at different concentration of aluminum (in the electrospinning solution).

Table 4. The micro-structural parameters of the four different nanofiber samples.

Sample	Lattice Parameters			Volume of the Unit Cell ( $\text{\AA}^3$ )
	a ( $\text{\AA}$ )	c ( $\text{\AA}$ )	c/a	
ZnO (Undoped)	3.249	5.205	1.602	47.583
AOZO1	3.244	5.186	1.599	47.263
AOZO2	3.242	5.195	1.602	47.287
AOZO3	3.241	5.209	1.607	47.385

Figure 3.9 shows the representative spectra for different aluminum oxide doped zinc oxide nanofiber samples. Based on these reflectance spectra, the absorption edge for each material was determined by the first derivative method. Using the calculated absorption edge values, the band gap energies

were calculated as 3.35 eV for undoped ZnO nanofibers and 3.12, 3.17, and 3.23 eV for the three doped AOZO nanofiber samples, respectively, using the relationship of photon energy and frequency  $E = h\nu$ , where  $h$  is Planck's constant ( $6.626 \times 10^{-34}$  J·s) and  $\nu = c/\lambda$ , where  $c$  is the speed of light ( $2.998 \times 10^8$  m/s) and  $\lambda$  is the wavelength of light. The optical bandgap of the four different samples are given in Table 5.

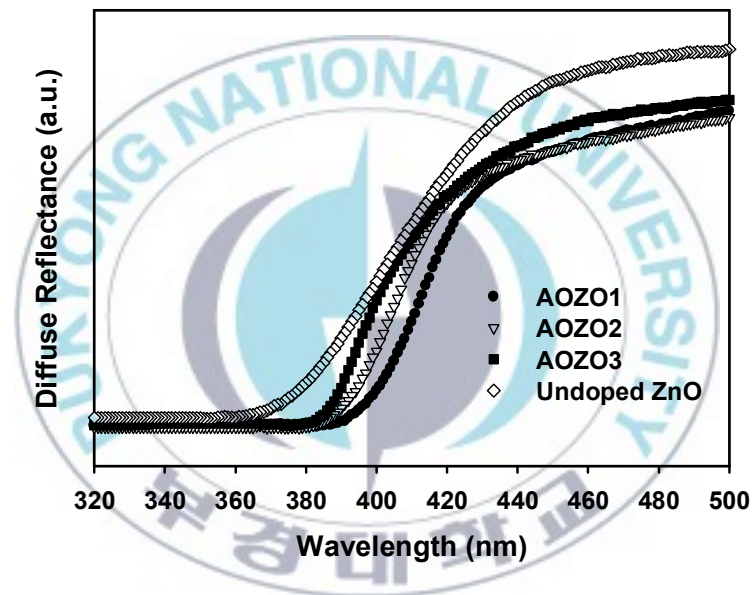


Figure 3.9. UV-Vis spectra of undoped and aluminum oxide doped zinc oxide nanofibers (calcined at 873 K for 5 hrs).

Table 5. Optical bandgap and conductivity of four different aluminum oxide doped zinc oxide (AOZO) nanofiber samples after calcining at 873 K for 5 hrs.

Sample	Atomic Ratio in Electrospinning Solution	Optical Bandgap (eV)	Conductivity $\times 10^3$ (S/cm)
ZnO (Undoped)	0	$3.35 \pm 0.02$	$0.02 \pm 0.002$
AOZO1	0.70	$3.12 \pm 0.01$	$2.45 \pm 0.08$
AOZO2	1.00	$3.17 \pm 0.02$	$1.93 \pm 0.11$
AOZO3	1.35	$3.23 \pm 0.01$	$1.54 \pm 0.07$

The conductivities ( $\sigma$ , S/cm) of the AOZO materials were calculated using the resistance  $R$  obtained from the I-V measurement, length  $L$ , and cross sectional area  $A$  of the disks as  $\sigma = L/RA$ . Figure 3.10 shows the conductivity of different AOZO nanofibers at room temperature. Compared to the undoped zinc oxide nanofibers with a conductivity of  $0.0199 \times 10^{-3}$  S/cm, the AOZO nanofibers exhibited two order of magnitude increase up to  $2.447 \times 10^{-3}$  S/cm (sample AOZO1). Further increase of aluminum content then decreased the conductivity of the nanofiber samples at room temperature.

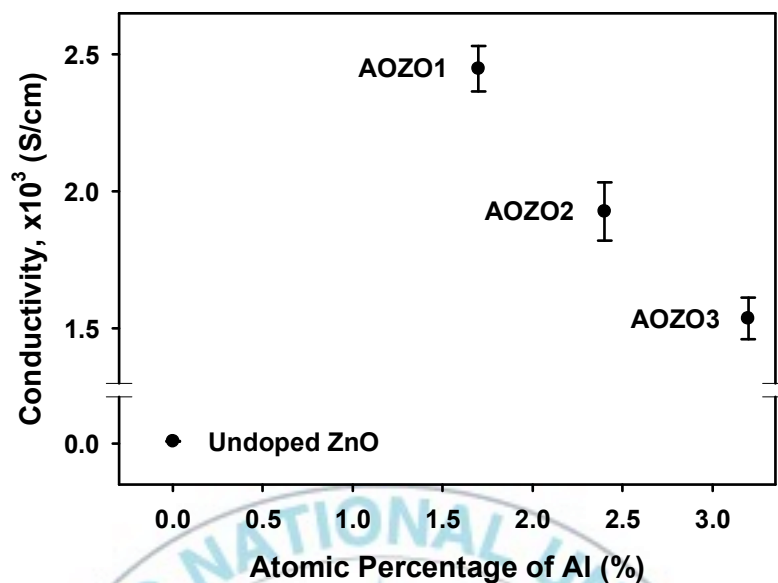


Figure 3.10. Electrical conductivities of undoped and aluminum oxide doped zinc oxide nanofibers (calcined at 873 K for 5 hrs).

High resolution XP spectra from undoped zinc oxide to the AOZO3 samples in the binding energy ranges of Zn 2p, O 1s, and Al 2s electrons are shown in Figure 3.11 (a), (b), and (c), respectively. The Al 2s region was chosen to analyze instead of the Al 2p since the latter overlapped with Zn 2p satellite peaks. Charging effects were corrected using the C 1s peak of drift carbon at 284.6 eV as a reference [52]. As the amount of aluminum dopant increased, the chemical environment of the electrospun zinc oxide nanofibers changed. The intensity of the high energy Zn 2p signatures increased as aluminum was added as shown in Figure 3.11 (a). The O 1s and Al 2s peak maxima were also observed to shift to higher binding energy as shown in Figures 3.11 (b) and (c), respectively. These peak shifts imply that the aluminum oxide dopant affects the chemical states of Zn, as well as O and Al,

with higher oxidation states developing as the amount of Al increases.

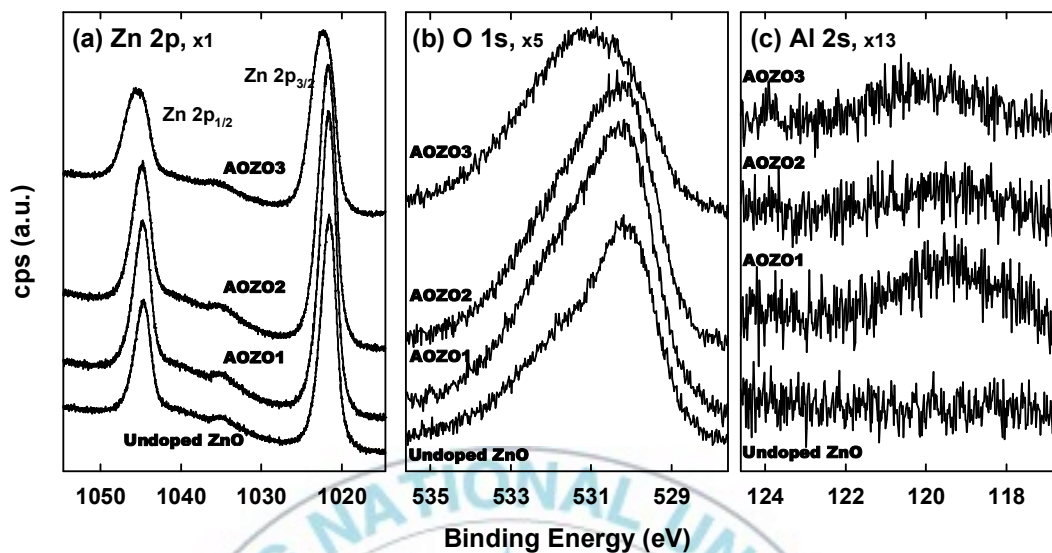


Figure 3.11. High resolution X-ray photoelectron spectra from undoped zinc oxide to AOZO3 of the Zn 2p region (a), O 1s region (b), and Al 2s region (c) from bottom to top.

The conductivity measurements in Figure 3.10 indicate that the aluminum content controls the conductivity of the AOZO nanofibers conducting a non-monotonic way. To better understand the chemical environment of the AOZO nanofibers, deconvolution of the XPS features in the three different regions of interest (Zn 2p, O 1s, and Al 2s) was performed using XPSPEAK shareware (ver. 4.1). The FWHMs used for peak deconvolution are 2.1-2.3, 2.0-2.5, and 1.9-2.2 for Zn 2p, Al 2s, and O 1s, respectively. The representative deconvoluted peaks of AOZO1 and AOZO3 are shown in Figure 3.12. Since the spin-orbit splitting constant of Zn 2p is so wide (22.97 eV), the deconvoluted Zn 2p<sub>3/2</sub> is shown in Figure 3.12 (a) instead of showing of the entire Zn 2p region. Two oxidation states were assigned for Zn species after

the deconvolution process; one for the metallic zinc at a binding energy of 1021.5 eV and one for zinc oxide at around 1022.8 eV. As the aluminum oxide as a dopant was increased, the ratio of metallic zinc to zinc oxide was decreased from 3.06 to 1.13.

The detailed chemical environment of oxygen is shown in Figure 3.12 (b). The assigned binding energies of oxygen for four different chemical environments are around 530.3 eV for ZnO [53,54], 531.5 eV for low binding energy aluminum oxide ( $\text{AlO}_x$ ), at 532.2 eV for surface hydroxide [55], and 533.7 eV for high binding energy aluminum oxide ( $\text{AlO}_y$ ), where the subscript  $x$  is smaller than  $y$ . The oxygen ratio of zinc oxide to aluminum oxide decreased from 2.29 to 1.35 as the aluminum content increased from the ratio of Al/Zn of 1.75 to 3.33 at.%. The three assigned aluminum species after deconvolution are metallic aluminum at 119.4 eV, low binding energy aluminum oxide at 119.9 eV, and high binding energy aluminum oxide at 121.0 eV denoted by  $\text{Al}^0$ ,  $\text{AlO}_x$ , and  $\text{AlO}_y$ , respectively, in Figure 3.12 (c). As shown in Figure 3.12 (a, b, c), increasing the amount of aluminum content in zinc oxide nanofibers caused an increase of ratio of Al/Zn from 0.058 to 0.064 and the oxide forms of both zinc and aluminum as well. However, the ratio of  $\text{Al}/(\text{AlO}_x+\text{AlO}_y)$  decreased from 1.10 to 0.32 and that of  $\text{Zn}/\text{ZnO}$  decreased from 3.06 to 1.13 also. This increase of aluminum oxide (at the expense of metallic Al) is believed to be the cause of the reduction in the electrical conductivity.

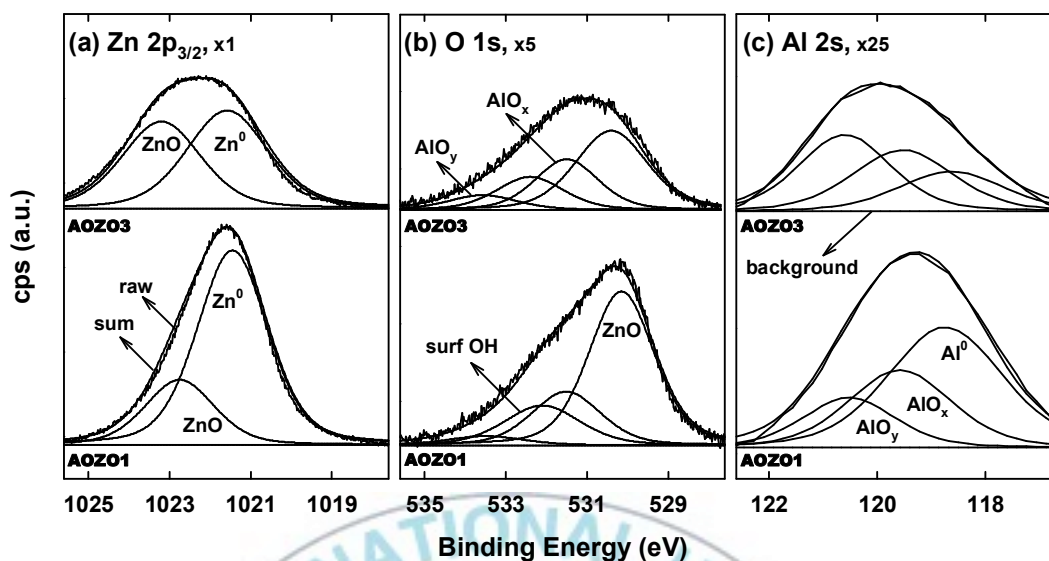


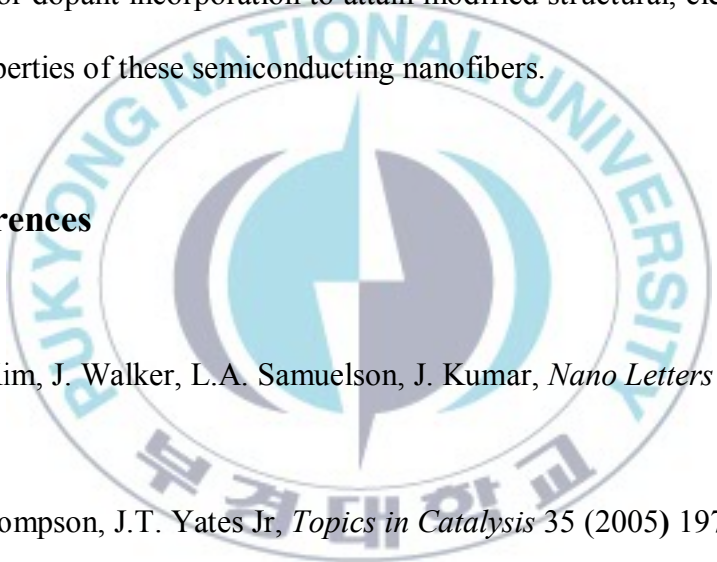
Figure 3.12. Representative deconvoluted X-ray photoelectron spectra AOZO1(bottom) and AOZO3(top) of the Zn  $2p_{3/2}$  region (a), O 1s region (b), and Al 2s region (c). In (a) metallic zinc at a binding energy of 1021.5 eV and zinc oxide at around 1022.8 eV are assigned. In (b) the assigned binding energies for oxygen are around 530.3 eV for ZnO, 531.5 eV for low binding energy aluminum oxide ( $AlO_x$ ), 532.2 eV for surface hydroxide, and 533.7 eV for high binding energy aluminum oxide ( $AlO_y$ ). In (c) metallic aluminum at 119.4 eV, low binding energy aluminum oxide at 119.9 eV, and high binding energy aluminum oxide at 121.0 eV denoted  $Al^0$ ,  $AlO_x$ , and  $AlO_y$  (where  $x < y$ ) are indicated.

### 3.2.4. Conclusion

Aluminum oxide doped zinc oxide (AOZO) nanofiber mats have been successfully prepared by electrospinning polymer solutions containing the sol-gel precursors and heating the fiber mats. The hexagonal wurtzite structure was not modified by the addition of dopant (aluminum oxide) at low concentration levels. While the incorporation of aluminum oxide dopant shifted the UV absorption edges to higher wavelength compared to undoped zinc oxide nanofibers, further addition of aluminum shifted the absorption

edges to the lower wavelength. Conductivity measurements showed that incorporation of dopant-aluminum at the 0.70 at. wt% level increased the conductivity of zinc oxide nanofibers two order of magnitude but further increases of aluminum decreased the conductivity. XPS investigations indicate that the conductivity of the AOZO samples was controlled by the relative amount of metallic aluminum present, and that this changes with continued doping. Electrospinning proved to be a simple, low cost, and reliable technique for dopant incorporation to attain modified structural, electrical, and optical properties of these semiconducting nanofibers.

### 3.3. References

- 
- [1] Y.-G. Kim, J. Walker, L.A. Samuelson, J. Kumar, *Nano Letters* 3 (2003) 523.
- [2] T.L. Thompson, J.T. Yates Jr, *Topics in Catalysis* 35 (2005) 197.
- [3] M.R. Mohammadi, D.J. Fray, M.C. Cordero-Cabrera, *Sens. Actuators, B* 124 (2007) 74.
- [4] K.M. Reddy, C.V. G. Reddy, S.V. Manorama, *J. Solid State Chem.* 158 (2001) 180.
- [5] M.-S. Kim, J.G. Chung, *J. Colloid Interface Sci.* 233 (2001) 31.
- [6] A. Jaroenworarluck, W. Sunsaneeyametha, N. Kosachan, R. Stevens, *Surf. Interface Anal.* 38 (2006) 473.
- [7] J. Zhang, M. Li, Z. Feng, J. Chen, C. Li, *J. Phys. Chem. B* 110 (2006) 927.

- [8] A.R. Gandhe, S.P. Naik, S.B. Kakodkar, J.B. Fernandes, *Cat. Commun.* 7 (2006) 285.
- [9] J.-M. Giraudon, T.B. Nguyen, G. Leclercq, S. Siffert, J.-F. Lamonier, A. Aboukaïs, A. Vantomme, B.-L. Su, *Catal. Today* 137 (2008) 379.
- [10] Y. Sun, T. Egawa, L. Zhang, X. Yao, *Jpn. J. Appl. Phys.* 41 (2002) L945.
- [11] S. H. Lim, N. Phonthammachai, T. Liu, T.J. White, *J. Appl. Cryst.* 41 (2008) 1009.
- [12] G. Hu, X. Meng, X. Feng, Y. Ding, S. Zhang, M. Yang, *J. Mater. Sci.* 42 (2007) 7162.
- [13] Y. Su, X. Zhang, S. Han, X. Chen, L. Lei, *Electrochem. Commun.* 9 (2007) 2291.
- [14] B. Xia, H. Huang, Y. Xie, *Mater. Sci. Eng. B* 57 (1999) 150.
- [15] K. Madhusudan Reddy, C.V. Gopal Reddy, S.V. Manorama, *J. Solid State Chem.* 158 (2001) 180.
- [16] C. Tekmen, A. Suslu, U. Cocen, *Mater. Letters* 62 (2008) 4470.
- [17] D.H. Reneker, A.L. Yarin, H. Fong, *J. Appl. Phys.* 87 (2000) 4531.
- [18] E.T. Bender, P. Katta, A. Lotus, *Chem. Phys. Lett.* 423 (2006) 302.
- [19] S.R. Dhage, S.P. Gaikwad, V. Ravi, *Bull. Mater. Sci.* 27 (2004) 487.
- [20] M. Gopel, W.J.M. Chan, L.C.D. Jonghe, *J. Mater. Sci.* 32 (1997) 6001.
- [21] B. Elsener, D. Atzei, A. Krolikowski, *Chem. Mater.* 16 (2004) 4216.
- [22] G. Srinivasan, R.T. Rajendra Kumar, J. Kumar, *Opt. Mater.* 30 (2007) 314.
- [23] Y. Li, G.W. Meng, L.D. Zhang, F. Phillipp, *Appl. Phys. Lett.* 76 (2000) 2011.

- [24] H.T. Ng, J. Han, T. Yamada, P. Nguyen, Y.P. Chen, M. Meyyappan, *Nano Lett.* 4 (2004) 1247.
- [25] Z.Y. Fan, D.W. Wang, P.C. Chang, W.Y. Tseng, J.G. Lu, *Appl. Phys. Lett.* 85 (2004) 5923.
- [26] A.E. Jimenez-Gonzalez, *J. Solid State Chem.* 128 (1997) 176.
- [27] K.L. Chopra, S. Major, D.K. Pandya, *Thin Solid Films* 102 (1983) 1.
- [28] C. Lee, K. Lim, J. Song, *Sol. Energy Mater. Sol. Cells* 43 (1996) 37.
- [29] L. Bahadur, M. Hamdani, J.F. Koenig, P. Chartier, *Sol. Energy Mater.* 14 (1986) 107.
- [30] T. Negami, Y. Hashimoto, S. Nishiwaki, *Sol. Energy Mater. Sol. Cells* 67 (2001) 331.
- [31] K. Matsubara, P. Fons, K. Iwata, A. Yamada, K. Sakurai, H. Tampo, S. Niki, *Thin Solid Films* 369 (2003) 431.
- [32] D.C. Look, D.C. Reynolds, C.W. Litton, R.L. Jones, D.B. Eason, G. Cantwell, *Appl. Phys. Lett.* 81 (2002) 1830.
- [33] R.M. Schaffert, *Electrophotography*, Focal Press, London, 1980, p. 320.
- [34] X. Wang, W.P. Careg, S. Yee, *Sens. Actuators B* 28 (1995) 63.
- [35] Z.C. Jin C.G. Granqvist, *Proc. SPIE* 21, 823 (1987).
- [36] H.S. Kang, J.S. Kang, J.W. Kim, S.Y. Lee, *J. Appl. Phys.* 95 (2004) 1246.
- [37] S.Y. Lee, Y. Li, J.-S. Lee, J.K. Lee, M. Nastasi, S.A. Crooker, Q.X. Jia, *Appl. Phys. Lett.* 85 (2004) 218.
- [38] K. Matsubara, P. Fons, K. Iwata, A. Yamada, K. Sakurai, H. Tampo, S. Niki, *Thin Solid Films* 431–432 (2003) 369.

- [39] S. Takeda, M. Fukawa, *Thin Solid Films* 468 (2004) 234.
- [40] F. Zhu, K. Zhang, E. Guenther, C.S. Jin, *Thin Solid Films* 363 (2000) 314.
- [41] R. Das, T. Jana, S. Ray, *Sol. Energy Mater. Sol. Cells* 86 (2005) 207.
- [42] K.-S. Kim, H.W. Kim, *Physica B* 328 (2003) 368.
- [43] M. Sano, K. Miyamoto, H. Kato, *J. Appl. Phys.* 95 (2004) 5527.
- [44] Y. Ma, G.T. Du, S.R. Yang, Z.T. Li, B.J. Zhao, X.T. Yang, T.P. Yang, Y.T. Zhang, D.L. Liu, *J. Appl. Phys.* 95 (2004) 6268.
- [45] J. Zhenguang, L. Kun, Y. Chengxing, F. Ruixin, Y. Zhizhen, *J. Cryst. Growth* 253 (2003) 246.
- [46] P. Nunes, E. Fortunato, P. Tonello, F. Braz Fernandes, P. Vilarinho, R. Martins, *Vacuum* 64 (2002) 281.
- [47] L. Armelao, M. Fabrizio, S. Gialaneela, F. Zordan, *Thin Solid Films* 394 (2001) 90.
- [48] C. Lorenz, A. Emmerling, J. Fricke, T. Schmidt, M. Hilgendorff, L. Spanhel, G. Muller, *J. Non-Cryst. Solids* 238 (1998) 1.
- [49] S. Chakrabarti, D. Das, D. Ganguli, S. Chaudhuri, *Thin Solid Films* 441 (2003) 228.
- [50] G. Srinivasan, J. Kumar, *Cryst. Res. Tech.* 41 (2006) 893.
- [51] JCPDS Database, International Center for Diffraction Data. (1986) Card No. 36-1451.
- [52] H.J. Borg, C.C.A. van den Oetelaar, L.J. van Ijendoorn, J.W. Niemantsverdriet, *J. Vac. Sci. Technol. A* 10 (1992) 2737.
- [53] G.L. Mar, P.Y. Timbrell, R.N. Lamb, *Chem. Mater.* 7 (1995) 1890.

[54] L.-J. Meng, C.P. Moreira de Sá, M.P. dos Santos, *Appl. Surf. Sci.* 78 (1994) 57.

[55] C.T. Au, M.W. Roberts, A.R. Zhu, *Surf. Sci.* 115 (1982) L117.



## CHAPTER 4. Investigation of Thin Films

### 4.1. XPS Investigation of Molybdenum Thin Films

#### 4.1.1. Introduction

The chalcopyrite  $\text{Cu(In,Ga)Se}_2$  (CIGS) and its alloys are of great interest in photovoltaic devices because of its high optical absorption coefficient and a direct band gap for solar radiation. Various back contact of CIGS films have different structural, optical, and electrical properties, which can affect the characteristics of CIGS films deposited on it [1,2]. One of the most promising material is molybdenum thin films with good electrical conductivity, chemical stability, low differential thermal expansion, and excellent substrate adhesion. Radio frequency (RF) (13.56 MHz) magnetron sputtering is a convenient techniques for depositing Mo thin films, and the effects of film thickness [3] and deposition conditions such as RF power, target-substrate distance and the argon pressure [4-6] have been studied. It has been shown that the increase in electrical resistivity (sheet resistance) of these films can logically be explained by the increased surface roughness [5] and decreased grain size [3], i.e. more grain boundaries and therefore more scattering centers. Mo films are typically deposited on the glass, which ideally presents an inexpensive, inert, and mechanically durable substrate at low temperatures [7]. Especially, it is well known that Na in the soda-lime glass substrates is

diffused into the CIGS films through the Mo back contact and then led to increase in the efficiency of solar cell upto 19.9% with sputtered Mo back contact [8] by substituting for Cu in the CIGS films [9].

In this work, we studied X-ray photoelectron spectroscopy (XPS) in both survey scan and high resolution modes on the Mo films deposited by RF magnetron sputtering on the soda-lime glass substrates to investigate and correlate changes in electrical resistivity with their chemical nature.

#### **4.1.2. Experimental Section**

Molybdenum thin films were deposited on ultrasonically cleaned soda-lime glass substrates by radio frequency magnetron sputtering using a high purity 5 cm diameter Mo target (99.95%). Films were prepared by changing argon pressure between 4 and 20 mTorr, while keeping a constant RF power of 100 W. The thickness was kept constant at 0.75  $\mu\text{m}$  by increasing the sputtering time with increasing argon pressure, due to higher sputtering rates at higher argon pressure. The deposition rate at 4 mTorr was 12.5 nm/min, whereas it was 9.4 nm/min at 20 mTorr. The substrates were not heated, even though an upward drift of the temperature during the sputtering process was observed, with a maximum temperature of 40°C. The deposition was performed under pure argon gas (99.998%) flowing at 10 sccm. Uniform films thickness ( $\pm 5\%$  uncertainty) was achieved using a rotatable substrate holder (12 rpm) fixed 6 cm away from the target.

The film thickness was measured by DekTak<sup>3</sup>ST surface profiler. The X-Ray diffraction (XRD) measurements were carried out using a XPERT-PRO diffractometer using Cu K $\alpha$ 1 radiation in scanning 2 $\theta$  mode

X-ray photoelectron spectroscopy (VG ESCALAB MK II) was used for investigating the chemical nature of the oxidation state and chemical composition of the deposited Mo thin films. The base pressure of the XPS chamber was less than  $1 \times 10^{-9}$  mbar. A twin anode X-ray source with Mg K $\alpha$  (1253.6 eV) and Al K $\alpha$  (1486.6 eV), and a concentric hemispherical analyzer (CHA) were housed in the XPS system. The XP spectra were taken using the Al K $\alpha$  X-ray source. Charging effects were corrected using the C 1s peak of drift carbon at 284.6 eV as a reference [10]. The parameters used for XPS experiments were an anode voltage of 9 kV, an electron multiplier voltage of 2850 eV, an anode current of 20 mA, a filament current of 4.2 A, a pass energy of 20 eV, a dwell time of 100 ms, and an energy step size of 0.02 eV in constant analyzer energy (CAE) mode for high resolution scans. And 0.5 eV of step size for survey scan was used and other parameters were the same as applied in the high resolution scans.

#### **4.1.3. Results and Discussion**

The XP survey spectra of five different samples made with different sputtering pressures are shown in Figure 4.1. The contents of Mo and oxygen increased from Mo-1 (4 mTorr of Ar pressure) to Mo-5 (20 mTorr of Ar pressure). The oxidation states of Mo consisted of metallic Mo, Mo<sup>4+</sup>, and

$\text{Mo}^{6+}$  and oxygen was found in the form of  $\text{MoO}_2$ ,  $\text{MoO}_3$ , and surface oxygen [11]. The detailed peak analyses of Mo and oxygen were performed by peak deconvolution using the XPSPEAK program with the results shown in Figures 4.2 and 4.3, respectively.

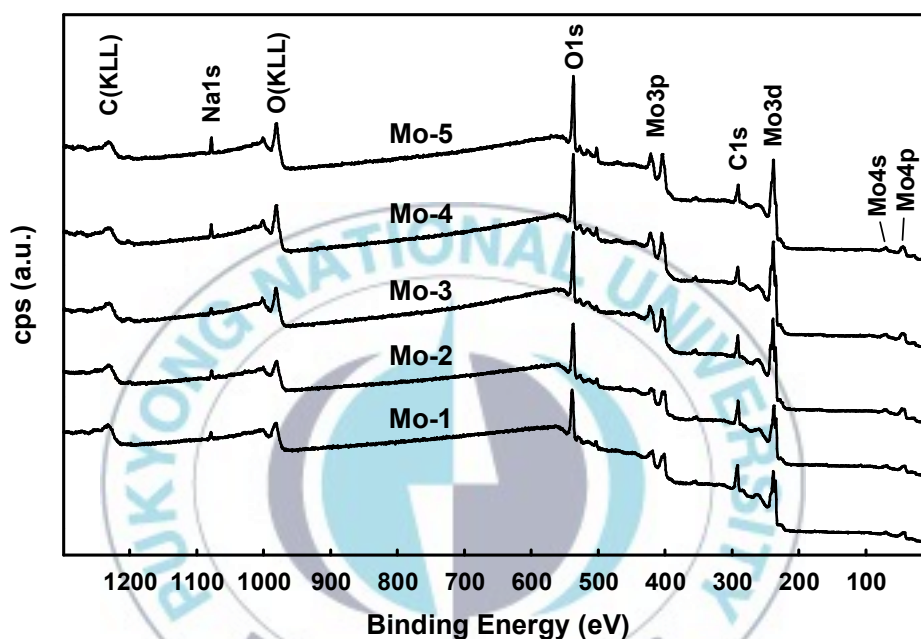


Figure 4.1. Survey scans of sputter deposited Mo thin films. The notations are Mo-1 for deposition at 4 mTorr, Mo-2 for 8 mTorr, Mo-3 for 12 mTorr, Mo-4 for 16 mTorr, and Mo-5 for 20 mTorr working pressure in the RF magnetron sputtering chamber.

Figure 4.2 (a) shows high resolution XP spectra of the Mo 3d region of five different samples and Figure 4.2 (b) shows the representative deconvolution results. These spectra were deconvoluted into metallic Mo ( $227.9 \pm 0.3$  eV),  $\text{Mo}^{4+}$  ( $229.4 \pm 0.4$  eV), and  $\text{Mo}^{6+}$  ( $232.2 \pm 0.4$  eV) species as shown in Figure 4.2 (b) using the Mo  $3d_{5/2}$  features with a 3.13 eV spin orbit

splitting. The binding energies used for the deconvolution process are in good agreement with results reported by other groups [12-18]. It is clear that as the Ar pressure increased, the ratio of  $\text{Mo}^{6+}$  species (denoted as **3**) increased at the expense of metallic Mo (denoted as **1**) with the  $\text{Mo}^{4+}$  (denoted as **2**) states remaining relatively constant.

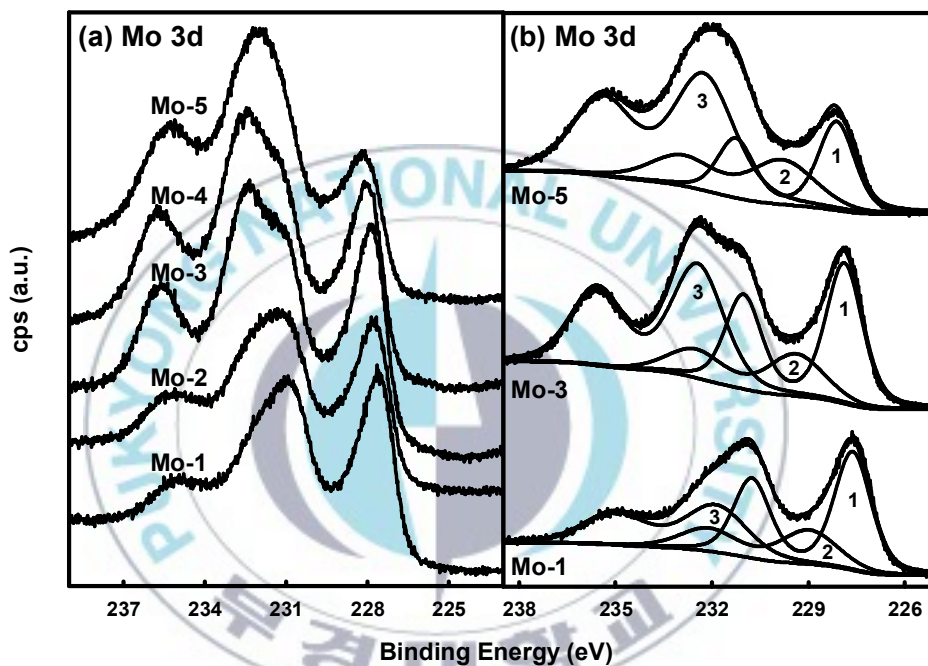


Figure 4.2. High resolution XP spectra of the Mo 3d range of Mo thin films. Mo 3d XP spectra of five different samples are stacked in Figure (a). Deconvoluted spectra of three representative samples are shown in figure (b). In figure (b), **1**, **2**, and **3** denote metallic Mo ( $\text{Mo}^0$ ),  $\text{Mo}^{4+}$ , and  $\text{Mo}^{6+}$ , respectively.

Figure 4.3 (a) contains high resolution XP spectra of the O 1s features with corresponding deconvolution results shown in Figure 4.3 (b). The deconvolution procedure included the three species assigned as O-surface ( $532.8 \pm 0.1$  eV) [11], O- $\text{Mo}^{4+}$  ( $531.5 \pm 0.3$  eV) and O- $\text{Mo}^{6+}$  ( $530.5 \pm 0.2$  eV),

respectively [13-18]. As the Ar pressure increased, the O-Mo<sup>6+</sup> (denoted as **1**) species increased but the O-Mo<sup>4+</sup> (denoted as **2**) states were not significantly affected, consistent with the results in Figure 4.2. The content of surface-O decreased until sample Mo-3 and then slightly increased up to Mo-5 as a function of Ar pressure.

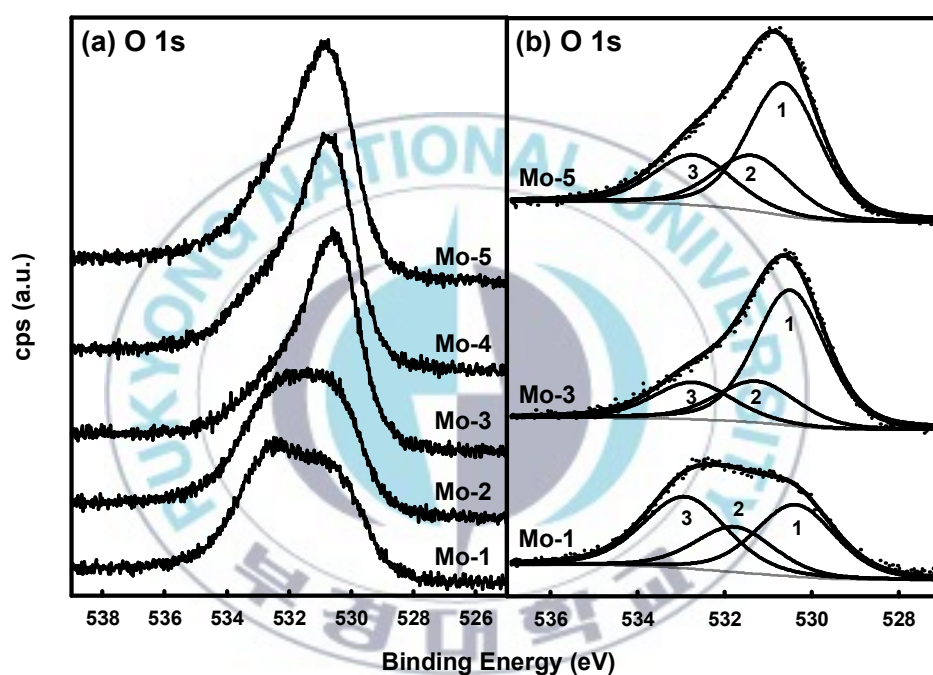


Figure 4.3. High resolution XP spectra of the O 1s range of Mo thin films. O 1s XP spectra of five different samples are stacked in figure (a). Deconvoluted spectra of three representative samples are shown in Figure (b). In figure (b), **1**, **2**, and **3** denote oxygen environments assigned to O-Mo<sup>6+</sup>, O-Mo<sup>4+</sup>, and surface oxygen, respectively.

After the soda-lime glass substrates were coated with Mo, the atomic percentage of Na at the surfaces varied in the range of 1.1 ~ 1.9 at.% depending on the sputtering conditions. From 4 mTorr (Mo-1) up to 12 mTorr

(Mo-3) the binding energy of the Na 1s electrons was constant but for higher sputtering pressures increased from 1071.6 eV to 1072.2 eV (Figure 3.9). Figure 4.4 shows the atomic percentages of Mo, O, and Na as a function of Ar sputtering pressure.

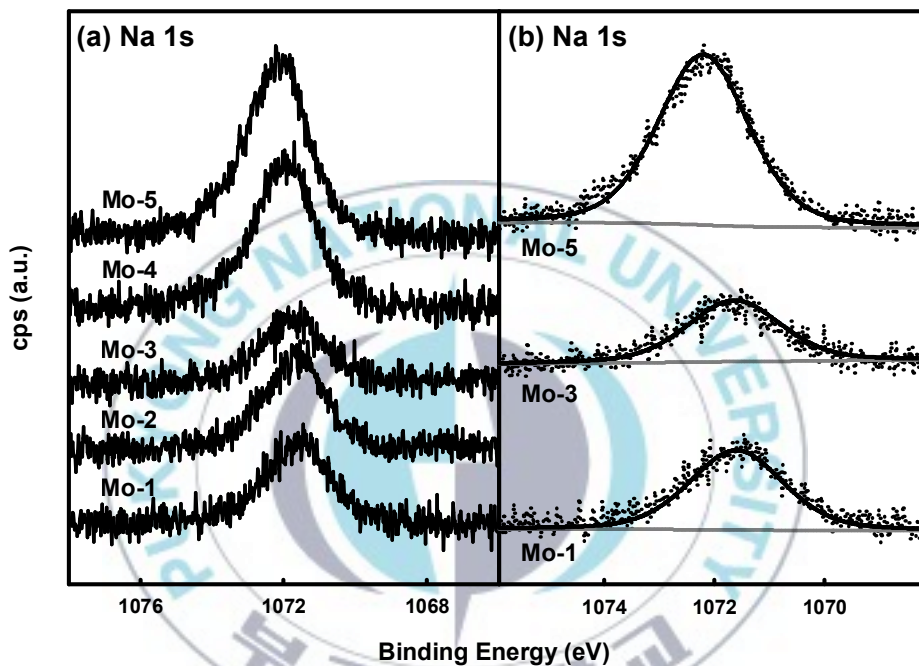


Figure 4.4. High resolution XP spectra of the Na 1s range of Mo thin films. Na 1s XP spectra of five different samples are stacked in Figure (a). Deconvoluted spectra of three representative samples are shown in figure (b).

Note in Figure 4.5 (b) that the relative percentage of oxygen detected is also a minimum at this sputtering pressure. However, Mo oxide formation as a function of Ar sputtering pressure is not consistent with the total atomic ratio of oxygen in Figure 4.5 (b); i.e. smaller amounts of oxygen produce more Mo oxides at the expense of metallic Mo. For clarity, the relative ratios of each

oxygen and Mo species are shown in Figures 4.6 (a) and 4.6 (b), respectively. Metallic Mo species decrease and Mo<sup>6+</sup> species increase monotonically as the sputtering pressure increases, and these trends do not appear to be sensitive to the maximum and minima exhibited in the data of Figure 4.5.

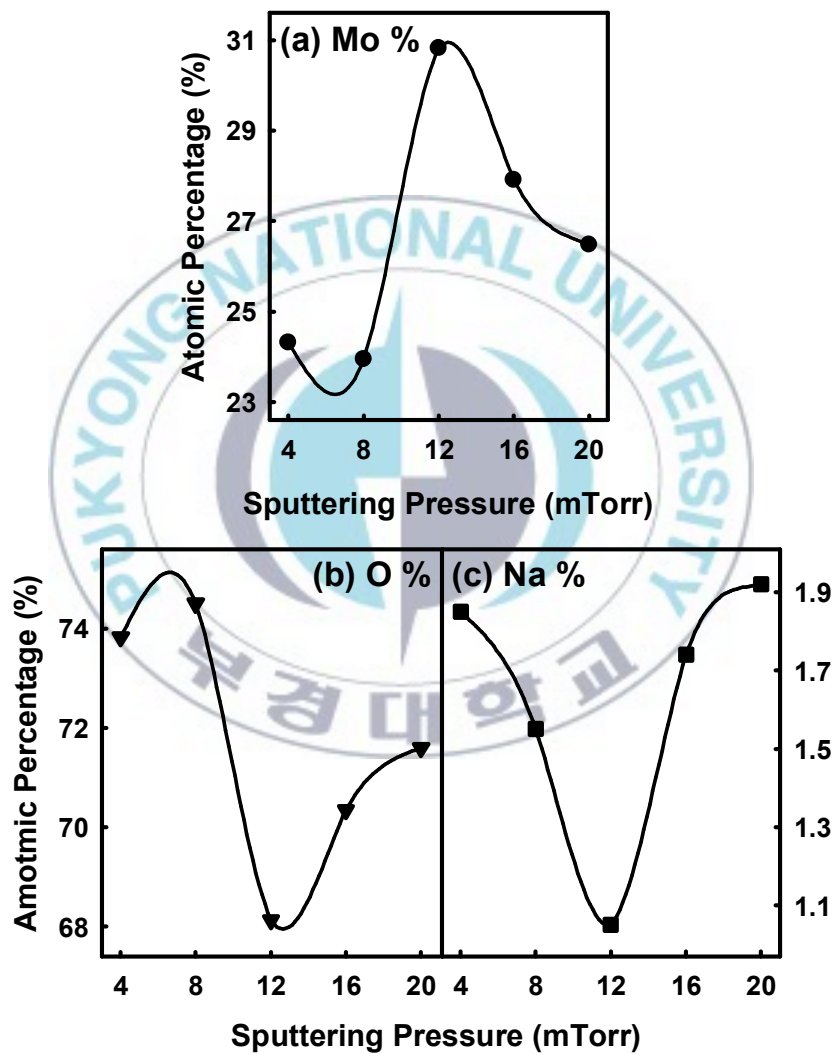


Figure 4.5. Atomic percentages of each element in the surface region of the Mo deposited thin films; molybdenum in (a), oxygen in (b), and sodium in (c).

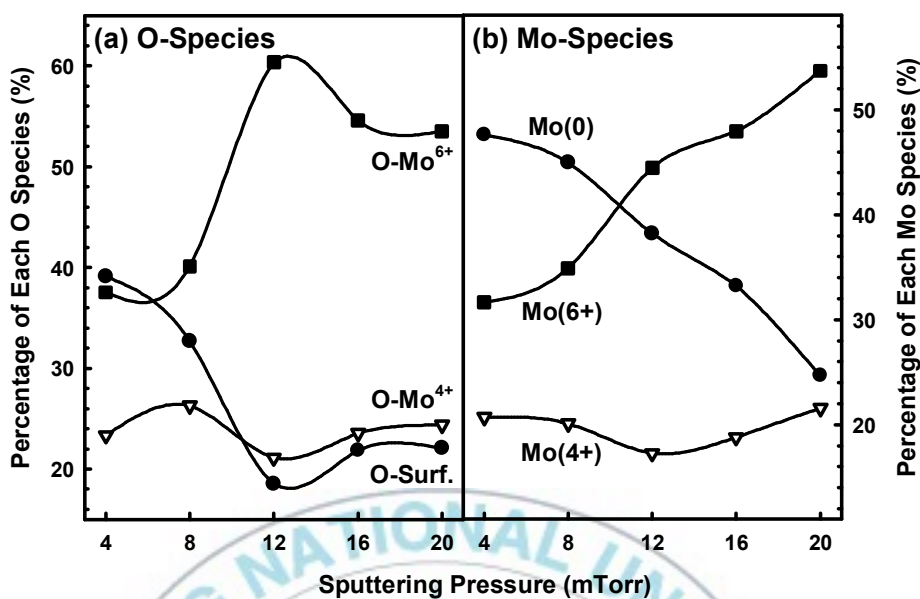


Figure 4.6. Atomic percentages of each chemical species of oxygen and molybdenum in (a) and (b), respectively.

It should be noted that XRD data (not shown) were dominated exclusively by Mo features, with no evidence for the existence of Mo oxides. This indicates that either these oxides are amorphous and therefore not able to produce diffraction maxima, or they exist only in the near surface region probed by XPS but not throughout the bulk of the films sampled by XRD. Since the surface properties of these thin films will ultimately determine their properties with respect to CIGS device functionality, it is therefore important that XPS has identified Mo oxides and surface contamination by sodium on the films that we studied.

It is clear from our results that Ar pressure differences during Mo sputtering influence more than the deposition rate of the target material on the

substrate. The proportion of oxygen-containing species in the background gas will depend on: the displacement of adsorbed gases from the chamber walls; the amount of carbon dioxide carried into the chamber as a common contaminant of Ar; the actual pumping speed of these species; and the substrate sputtering rate. All of these will be affected by the Ar pressure. Based on the data presented in Figure 4.5, it is most logical to conclude that the primary effect is the latter; i.e. that substrate sputtering is minimized at 12 mTorr of Ar pressure thereby minimizing the resulting amounts of sodium and oxygen at the surface (and possibly within the bulk) of the Mo films. As our XPS chamber is not equipped with well-controlled depth profiling capabilities, we did not pursue studies to investigate the interior of the films. What is most important, however, is the identification of sodium and molybdenum oxides on these films, which will affect their surface roughness and electrical properties as well as the adhesion and interfacial chemistry during CIGS fabrication.

#### **4.1.4. Conclusion**

Sputter deposited Mo thin films for CIGS applications on soda-lime glass have been studied by X-ray photoelectron spectroscopy. It is found that the Ar gas pressure used for sputtering affects the relative proportion of metallic and oxidized Mo species at the surface. Metallic Mo decreases monotonically with increasing sputtering pressure whereas Mo<sup>6+</sup> moieties increase. In comparison, the presence of Mo<sup>4+</sup> species is not significantly affected by changes in

sputtering conditions. In addition, sodium, sputtered from the substrate, is also found at the surface of the Mo thin films in varying amounts that depend on Ar pressure. These changes in surface stoichiometry are not accessible through XRD measurements and may influence the interfacial properties and functionalities of the resulting CIGS devices.

## **4.2. Properties of Zirconium Oxide Thin Films with Different Plasma Gas Ratio**

### **4.2.1. Introduction**

Zirconium oxide thin films are of interest on account of their excellent properties such as large resistance against oxidation, low thermal conductivity, high dielectric constant, and high refractive index. This material has been employed as many applications, which include catalysts [19] optical filters [20], resistive oxygen gas sensors [21]. In addition, ZrO<sub>2</sub> thin films have been considered to be replaced material which SiO<sub>2</sub> as the high *k* dielectric in the metal-oxide-semiconductor transistor [22]. These applications have led to various techniques to synthesize zirconium oxide thin films including d.c. reactive magnetron sputtering [23,24], chemical vapor deposition [25,26], sol-gel techniques [20,27], pulsed ion beam evaporation [28], liquid phase deposition [29], and filtered cathodic vacuum arc [30]. Radio frequency (RF) reactive magnetron sputtering is a widely used technique which is affected by

several deposition conditions, such as the RF power, mixing ratio of plasma gas, substrate temperature. Ma et al. have produced zirconium oxide thin films by RF reactive sputtering at different argon-oxygen atmosphere [31]. They investigated the dielectric characteristics of the  $ZrO_2$  film. Gao group studied the influence of the  $O_2$  gas concentration on the optical properties, residual stress, and microstructure of the  $ZrO_2$  thin films [32]. However, the chemical properties of the RF sputtered zirconium oxide thin films have been seldom reported. We studied the effects of the  $O_2$  ratio in the sputtering gases on the thickness, structure, and roughness of the deposited zirconium oxide thin films and oxidation state of elements in the films.

In the present work, we report the synthesis of zirconium oxide thin films by RF magnetron sputtering. We present the results of investigation into how the oxygen flow rate in the range at 0-80% affect physical and chemical properties of the zirconium oxide thin films. The chemical environment of the thin films was studied by means of X-ray photoelectron spectroscopy (XPS). Structural analysis of the zirconium oxide thin films was performed by atomic force microscopy (AFM) and X-ray diffraction (XRD) techniques. The film thickness was also investigated by spectroscopic ellipsometer (SE).

#### **4.2.2. Experimental Section**

Zirconium oxide thin films were deposited on p-type Si (100) wafer at room temperature using reactive RF (13.56 MHz) magnetron sputtering method in various oxygen mixing ratios. A zirconium target with a diameter of

2 inch was used for thin film deposition. The Si substrate was placed on the sample holder located 58 mm from the target. The chamber was pumped down below  $5.0 \times 10^{-7}$  Torr of base pressure, and the working pressure was kept about 45.5 mTorr. The argon and oxygen gases with purity of 99.999% fed into the vacuum chamber by standard mass flow controllers separately. The total flow rate was kept constant at 20 sccm, the oxygen mixing ratio was calculated that the O<sub>2</sub> flow rate divided by the total (Ar + O<sub>2</sub>) flow rate, and the values varied from 0 to 100%. The deposition conditions applied in this study are summarized in Table 6.

Table 6. The deposition parameters for RF sputtered zirconium oxide thin films.

Target	Zirconium
Substrate	Si wafer
Sputtering pressure	~ 45.5 mTorr
Base pressure	< $5.0 \times 10^{-7}$ Torr
Forward power	20 W
Reflected power	< 4W
Substrate temperature	Room temperature
Pre-sputtering time	1 hr
Sputtering time	3 hr

The morphology of the zirconium oxide thin films were checked with atomic force microscope (AFM, Veeco Multimode Digital Instruments Nanoscope III $\alpha$  system). The roughness of the films was measured as root mean square (rms) values. The XRD (PHILIPS, Netheland, X'Pert-MPD System) experiment was performed for phase identification with glancing

mode. The thickness of the zirconium oxide films was measured with the spectroscopic ellipsometry (SE) method.

Chemical characterization of the zirconium oxide films was carried out by X-ray photoelectron spectroscopy (XPS, THERMO VG SCIENTIFIC, UK, MultiLab2000), applying a monochromated Al K $\alpha$  X-ray source (1486.6 eV). The survey XP spectra were obtained with a concentric hemispherical analyzer (CHA) in constant analyzer energy (CAE) mode with a pass energy of 50 eV and an energy step size of 0.5 eV. High resolution XP spectra of Zr 3d and O 1s were obtained at a pass energy of 20 eV, an energy step size of 0.05 eV steps, and other parameters were kept the same as those applied in the survey scan. The spectra of Zr 3d and O 1s were deconvoluted by XPSPEAK software (ver 4.1) with Gaussian/Lorentzian ratio was 30% for the specific information of the oxidation states of the both elements and the ratios of the zirconium oxide surfaces.

#### **4.2.3. Results and Discussion**

The thickness of deposited zirconium oxide thin films by RF magnetron sputtering was measured by spectroscopic ellipsometer as shown in Figure 4.7. This result is consistent with the previous investigation by Anderle's group that the deposition rate is affected by sputtering mixture ratio [33]. In the plasma gas used to deposit zirconium oxide thin film, the argon ions are acted to sputter the zirconium particles from the target and the oxygen ions are acted as reactive species to form oxide. The sputtering yield is decreased, as the

percentage of the oxygen gas is increased, especially this effect is severe at the oxygen concentration is above 73% [31]. Also zirconium oxide layer deposited at the initial stage leads to a decrease of sputtering yield. Therefore, in general, the thickness of zirconium oxide thin films is decreased with increasing  $O_2$  concentration in the mixed sputter gas. The thickness of the zirconium oxide thin films at the 20% percent of  $O_2$  gas was thicker than other samples in this study. It could be caused by the loosely packed structure of the thin films [32].

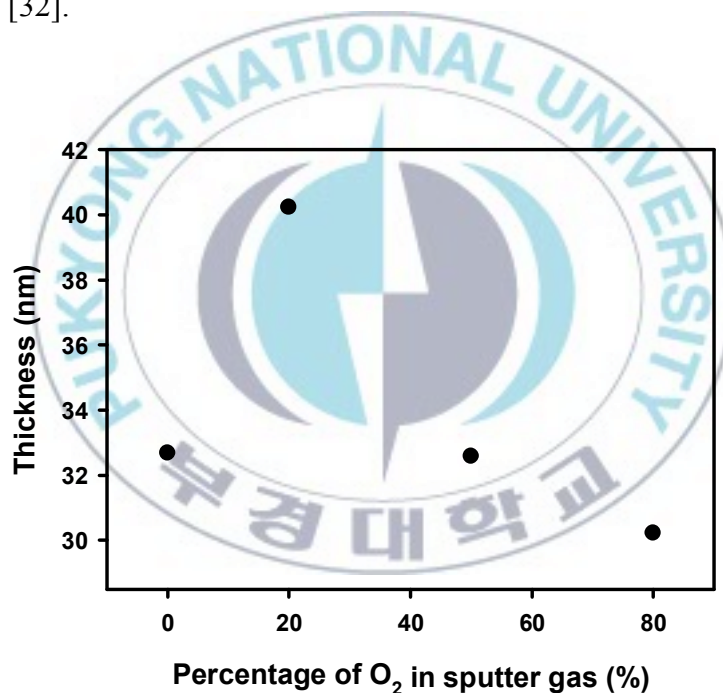


Figure 4.7. The thickness of the zirconium oxide thin films with different percentage of  $O_2$  in the sputter gas.

X-ray diffraction patterns of zirconium oxide thin films are shown in Figure 4.8. The notation of the samples is presented by  $O_2$ -number, for example,  $O_2$ -12 which is located at the right side of the graph means that the oxygen gas flow rate kept 12, the argon gas flow rate was 8 sccm and the total

gas flow rate was 20 sccm constantly. The crystalline  $ZrO_2$  generally can form monoclinic (m), tetragonal (t), cubic (c) phases, or orthorhombic (o) phase depending on the substrate temperature [34]. The stable crystal structure is monoclinic phase zirconia at room temperature. In our study, two peaks were observed at about  $38.5^\circ$  and  $58.5^\circ$ , which correspond to (101) planes of  $\alpha$ -Zr single crystal [35] and  $m-ZrO_2(-131)$ , respectively [36]. The zirconium oxide thin films prepared by RF magnetron sputtering were polycrystalline phases, those were Zr single crystal and monoclinic zirconia. The relative intensity of  $m-ZrO_2(-131)$  is stronger than that of Zr(101) except when the  $O_2$  gas was zero. The dominant phase in the range of above 20% of  $O_2$  gas concentration was the  $m-ZrO_2(-131)$ . No remarkable change of intensity of Zr(101) peak were observed varying the  $O_2$  gas concentration. On the other hand, the crystallization of the  $m-ZrO_2(-131)$  was dependent on the  $O_2$  concentration. The propensity of formation of zirconia crystal was increased as increasing  $O_2$  gas concentrations. As the concentration of  $O_2$  increased, monoclinic  $ZrO_2(-131)$  phase was increased while crystalline metallic Zr was saturated at zero  $O_2$  concentration [37]. Therefore, the oxygen ratio in the sputter gas was an important role of the synthesis of zirconium oxide thin film.

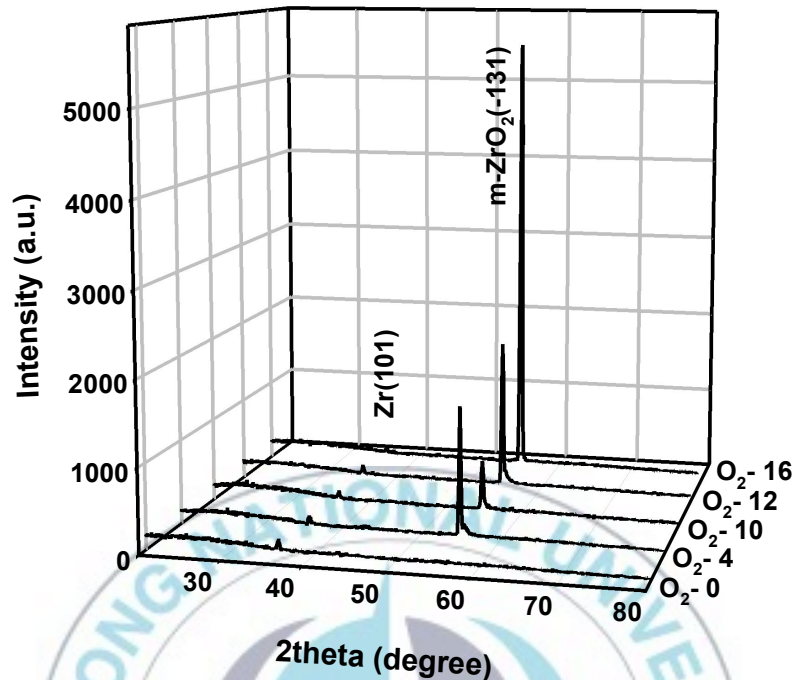


Figure 4.8. The XRD patterns of the zirconium oxide thin films on Si(100). The notation of the thin films is represented by O<sub>2</sub>-number. In O<sub>2</sub>-4, the number 4 indicates that the O<sub>2</sub> gas flow rate was 4 sccm and the total gas flow rate (O<sub>2</sub>+Ar) was constant at 20 sccm.

Figures 4.9 (a) and (b) show the representative high resolution XP spectra of Zr 3d and O 1s region of deposited zirconium oxide thin films with various O<sub>2</sub> gas concentrations. Two peaks of Zr 3d spectra are corresponded to the Zr 3d<sub>5/2</sub> and Zr 3d<sub>3/2</sub> with the spin-orbit splitting of 2.4 eV [38]. The doublet Zr 3d peaks of deposited zirconium oxide thin films were observed about 181.2 eV and 183.6 eV caused by bonding with oxygen [39]. In Figure 4.9 (b), the binding energy of O 1s for Si wafer was observed at 531.7 eV and that from zirconium oxide thin films coated on Si was dramatically decreased and the O 1s binding with zirconium was located about 529.6 eV. The XPS results

revealed that the deposition of zirconium oxide on the Si(100) wafers was successfully performed. And this was supported by XRD experiment shown in Figure 4.8. The comparison in FWHM (full width half maximum) of Zr 3d peaks and O 1s with different O<sub>2</sub> gas concentration suggests that more than two oxidation states are existed. The Zr 3d and O 1s spectra are deconvoluted in order to the better understanding of the chemical environment of zirconium oxide film and the effect of oxygen concentrations in Ar/O<sub>2</sub> mixture.

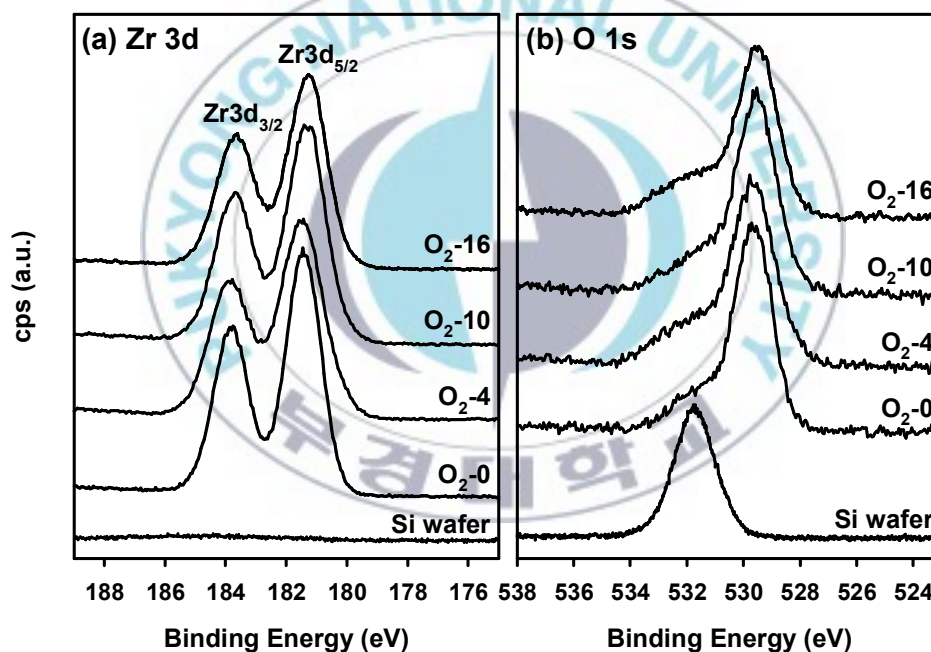


Figure 4.9. (a) Zr 3d and (b) O 1s XP spectra of zirconium oxide thin films prepared at different O<sub>2</sub> concentration.

Figures 4.10 show representative deconvolution spectra of Zr 3d and O 1s regions. The dotted line presents raw data obtained from XPS and the solid line overlapped with dotted line is the reconstructed data from the sum of individual peaks. In our study, three components are assigned in the Zr 3d XP

spectra. The formation of zirconium oxide was observed at the binding energy of 181.96 eV for Zr 3d<sub>5/2</sub> which is very close to the that of Zr<sup>4+</sup> in ZrO<sub>2</sub> [40]. And the higher and lower oxidation states of zirconium (ZrO<sub>x,y</sub> x,y<2, and x>y) [41] as zirconium suboxides were observed with a Zr 3d<sub>5/2</sub> binding energies at 181.27 eV and 180.72 eV, respectively. The ZrO<sub>2</sub> peak intensity is increased by compensating from higher oxidation state (ZrO<sub>x</sub>) to zirconia as the O<sub>2</sub> concentrations is increased. Figures 4.10 (d)-(e) represent the deconvolution spectra of O 1s. The O 1s fitting was performed with four oxygen components, the main peak consists of two components which are ZrO<sub>2</sub> at 529.24 eV and zirconium suboxide (ZrO<sub>x,y</sub>) at 529.84 eV [40]. The tail of the spectra contains chemisorbed OH groups (surf-O) and the oxygen bonded with Si(100) substrate (Si-O) at 531.43 eV [40] and 532.63 eV, respectively. The surface oxygen, which was no interaction with zirconium, seems to independent on the O<sub>2</sub> concentration. On the other hand, the intensities of zirconium suboxides were decreased and that of ZrO<sub>2</sub> was increased which is in good agreement with the data from deconvolution of Zr 3d spectra.

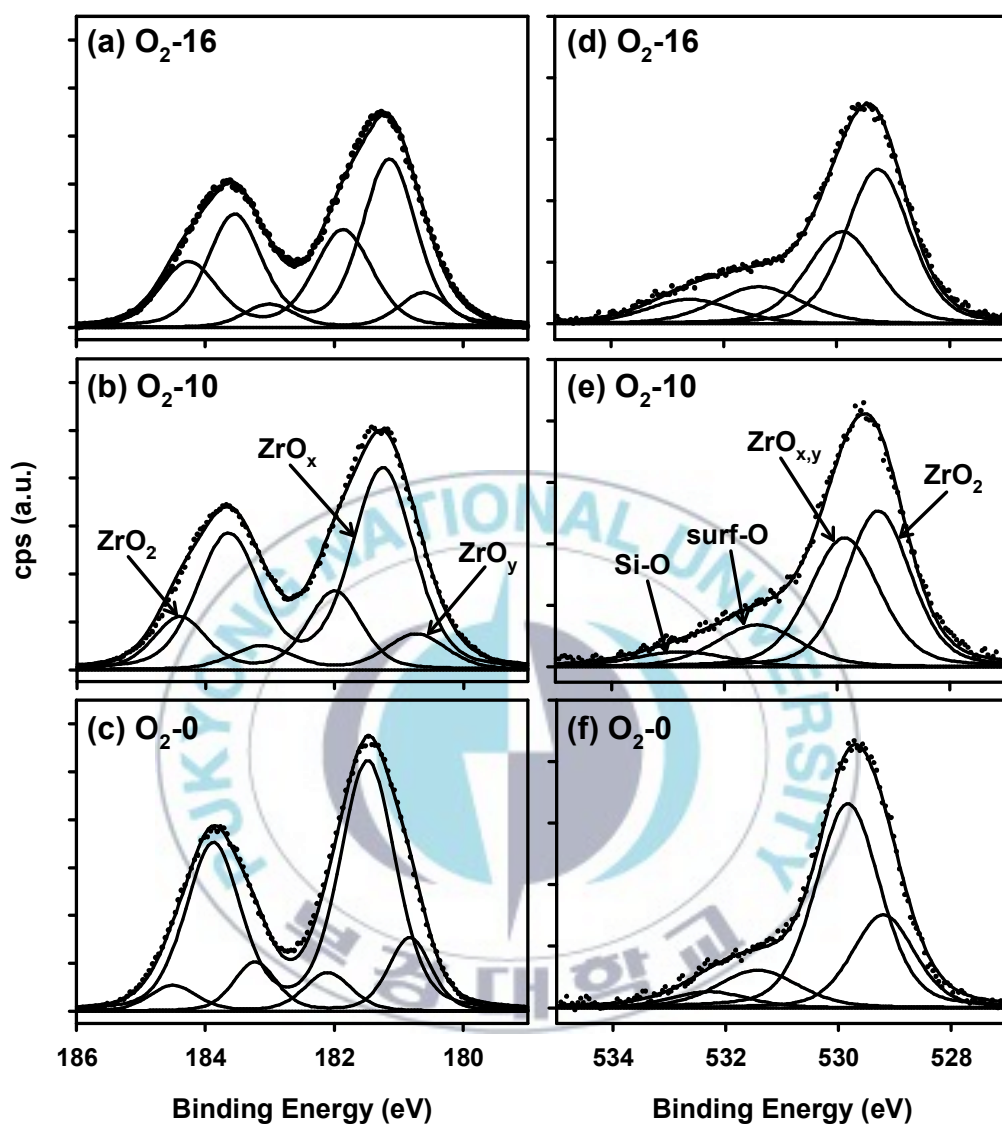


Figure 4.10. Deconvoluted XP spectra of Zr 3d: O<sub>2</sub>-16 (a), O<sub>2</sub>-10 (b), and O<sub>2</sub>-0 (c) and O 1s: O<sub>2</sub>-16 (d), O<sub>2</sub>-10 (e), and O<sub>2</sub>-0 (f).

The relative amounts of different zirconium and oxygen species in the films were calculated with their respective peak areas considering atomic sensitivity factors to obtain more accurate information shown in Figure 4.11 (a) and (b), respectively. The ratios of Zr and O species are quite different depending on the percentage of O<sub>2</sub> in the sputter gas as mentioned previously. The higher oxidation states of zirconium oxide (ZrO<sub>x</sub>) was decreased from 72.5% to 55.6% with increasing O<sub>2</sub> concentration and the zirconia form was increased from 9.3% to 34% and the ratio of the lower oxidation states (ZrO<sub>y</sub>) at 80% of O<sub>2</sub> in sputter gas was 7% less than that of 0% of O<sub>2</sub> concentration. It revealed that the higher oxidation state is easier to change zirconia form and has also been found in the study of the effect of different substrate temperatures on the zirconium oxide thin films [40]. It could be explained by that the higher oxidation state needs less energies to transform into more stable zirconia state in monoclinic structure. Note that the ratios of oxygen species showed the same trend with Zr species.

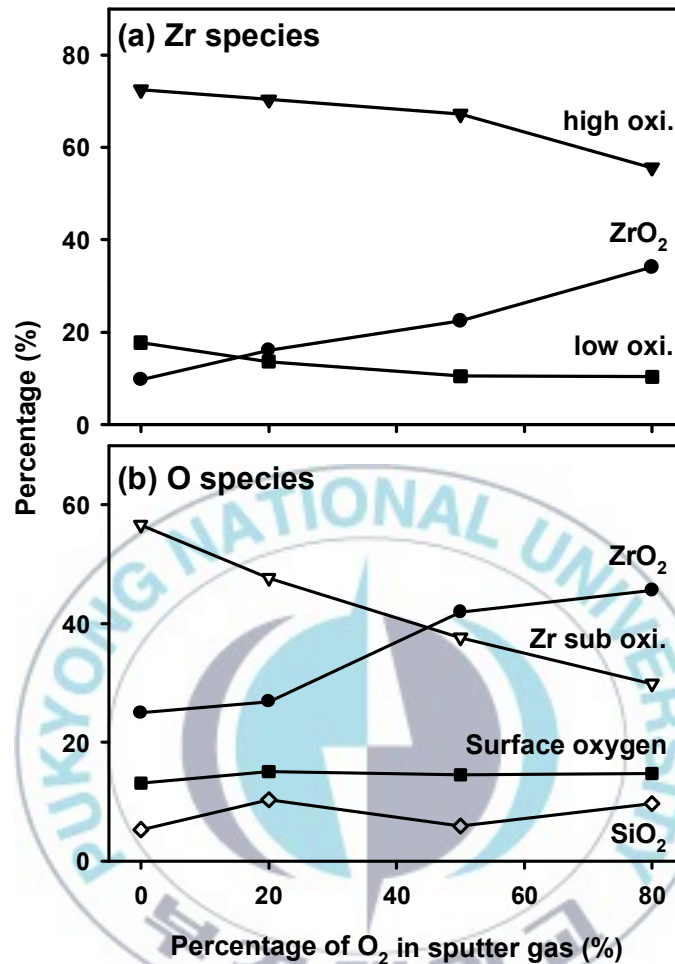


Figure 4.11. The relative ratios of (a) Zr species and (b) O species of different percentage of O<sub>2</sub> in sputter gas.

#### 4.2.4. Conclusion

Zirconium oxide thin films were deposited on the p-type Si(100) substrates by radio-frequency (RF) reactive magnetron sputtering with different plasma gas ratios. The monoclinic zirconium oxide thin films coexisted with Zr single crystal were obtained with mixed sputter gas including O<sub>2</sub> gas. The XP spectra showed that zirconium suboxide was

oxidized to the zirconia as increasing O<sub>2</sub> concentration. And the thickness of deposited thin film was in the range of 30~40 nm varying O<sub>2</sub> concentration.

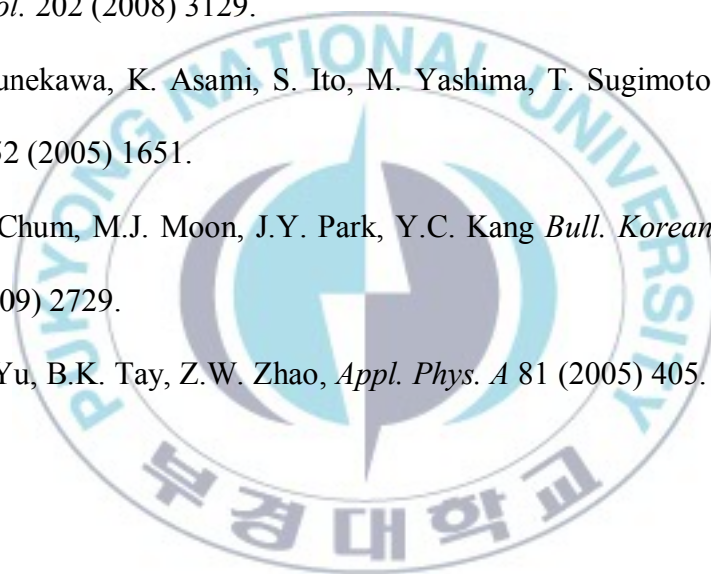
### 4.3. References

- [1] J.H. Yun, K.H. Kim, M.S. Kim, B.T. Ahn, S.J. Ahn, J.C. Lee, K.H. Yoon, *Thin Solid Films* 515 (2007) 5876.
- [2] T. Nakada, *Thin Solid Films* 480-481 (2005) 419.
- [3] Y. Kamikawa-Shimizu, S. Shimada, M. Watanabe, A. Yamada, K. Sakurai, S. Ishizuka, H. Komaki, K. Matsubara, H. Shibata, H. Tampo, K. Maejima, S. Niki, *Phys. Status Solidi A* 206 (2009) 1063.
- [4] L. Assmann, J.C. Bernède, A. Drici, C. Amory, E. Halgand, M. Morsli, *Appl. Surf. Sci.* 246 (2005) 159.
- [5] Ch. Dikov, M. Marinov, H. Maciel, K. Grigorov, I. Nedkov, G. Beshkov, *J. Optoelectron. Adv. M.* 7 (2005) 385.
- [6] M.A. Martínez, C. Guillén, *Surf. Coat. Technol.* 110 (1998) 62.
- [7] K. Granath, A. Rockett, M. Bodegard, C. Nender, L. Stolt, in *Proceedings of the 13th European Photovoltaic Solar Energy Conference*, edited by W. Freiesleben, H.S. Stephens and Associates, Bedford, 1995, p. 1983.
- [8] I. Repins, M.A. Contreras, B. Egaas, C. DeHart, J. Scharf, C.L. Perkins, B. To, R. Noufi, *Prog. Photovolt: Res. Appl.* 16 (2008) 235.

- [9] J. Hedstrom, H. Ohlsen, M. Bodegard, A. Kylner, L. Stolt, D. Hariskos, M. Ruckh, H.W. Schock, in *Proceedings of the 23th IEEE Photovoltaic Specialists Conference*, IEEE, New York, 1993, p 364.
- [10] H.J. Borg, C.C.A. van den Oetelaar, L.J. van Ijzendoorn, J.W. Niemantsverdriet, *J. Vac. Sci. Technol. A* 10 (1992) 2737.
- [11] C.T. Au, M.W. Roberts, A.R. Zhu, *Surf. Sci.* 115 (1982) L117.
- [12] Á. Koós, A. Oszkó, F. Solymosi, *Appl. Surf. Sci.* 253 (2007) 3022.
- [13] Z. Song, T. Cai, Z. Chang, G. Liu, J.A. Rodriguez, J. Hrbek, *J. Am. Chem. Soc.* 125 (2003) 8059.
- [14] F. Ruiz, Z. Benzo, M. Quintal, Á. Garaboto, A. Albornoz, J.L. Brito, *Appl. Surf. Sci.* 252 (2006) 8695.
- [15] T. Schroeder, J. Zegenhagen, N. Magg, B. Immaraporn, H.-J. Freund, *Surf. Sci.* 552 (2004) 85.
- [16] G.T. Kim, T.K. Park, H. Chung, Y.T. Kim, M.H. Kwon, J.G. Choi, *Appl. Surf. Sci.* 152 (1999) 35.
- [17] J.G. Choi, L.T. Thompson, *Appl. Surf. Sci.* 93 (1996) 143.
- [18] F. Werfel, E. Minni, *J. Phys. C: Solid State Phys.* 16 (1983) 6091.
- [19] T.M. Miller, V.H. Grassian, *J. Am. Chem. Soc.* 117 (1995) 10969.
- [20] Q. Zhang, X. Li, J. Shen, G. Wu, J. Wang, L. Chen, *Mater. Lett.* 45 (2002) 311.
- [21] N. Izu, W. Shin, I. Matsubara, N. Murayama, N. Oh-hori, M. Itou, *Sens. Actuators B* 108 (2005) 216.

- [22] M. Filipescu, N. Scarisoreanu, V. Craciun, B. Mitu, A. Purice, A. Moldovan, V. Ion, O. Toma, M. Dinescu, *Appl. Surf. Sci.* 253 (2007) 8184.
- [23] S. Venkataraj, O. Kappertz, C. Liesch, R. Detemple, R. Jayavel, M. Wuttig, *Vacuum* 75 (2004) 7.
- [24] Z. Ji, J.A. Haynes, M.K. Ferber, J.M. Rigsbee, *Surf. Coat. Technol.* 135 (2001) 109.
- [25] A.M. Torres-Huerta, M.A. Domínguez-Crespo, E. Ramírez-Meneses, J.R. Vargas-García, *Appl. Surf. Sci.* 255 (2009) 4792.
- [26] Y. Komatsu, T. Sato, S. Ito, K. Akashi, *Thin Solid Films* 341 (1999) 132.
- [27] R. Brenier, J. Mugnier, E. Mirica, *Appl. Surf. Sci.* 143 (1999) 85.
- [28] H. Suematsu, T. Kishi, J. Inoue, M. Hirai, T. Suzuki, T. Yunogami, W. Jiang, K. Yatsui, *Mater. Lett.* 61 (2007) 3635.
- [29] J.M. Lin, M.C. Hsu, K.Z. Fung, *J. Power Sources* 159 (2006) 49.
- [30] D.H.C. Chua, W.I. Milne, Z.W. Zhao, B.K. Tay, S.P. Lau, T. Carney, R.G. White, *J. Non-Cryst. Solids* 332 (2003) 185.
- [31] C.Y. Ma, F. Lapostolle, P. Briois, Q.Y. Zhang, *Appl. Surf. Sci.* 253 (2007) 8718.
- [32] P. Gao, L.J. Meng, M.P. Santos, V. Teixeira, M. Andritschky, *Vacuum* 56 (2000) 143.
- [33] G. Gottardi, N. Laidani, V. Micheli, R. Bartali, M. Anderle, *Surf. Coat. Technol.* 202 (2008) 2332.
- [34] K. Koski, J. Hölsä, P. Juliet, *Surf. Coat. Technol.* 120-121 (1999) 303.

- [35] JCPDS Database, International Center for Diffraction Data. (2003) Card No. 89-4902.
- [36] JCPDS Database, International Center for Diffraction Data. (2003) Card No. 83-0944.
- [37] M.S. Wong, W.J. Chia, P. Yashar, J.M. Schneider, W.D. Sproul, S.A. Barnett, *Surf. Coat. Technol.* 86-87 (1996) 381.
- [38] M. Matsuoka, S. Isotani, W. Sucasaire, N. Kuratani, K. Ogata, *Surf. Coat. Technol.* 202 (2008) 3129.
- [39] S. Tsunekawa, K. Asami, S. Ito, M. Yashima, T. Sugimoto, *Appl. Surf. Sci.* 252 (2005) 1651.
- [40] M.S. Chum, M.J. Moon, J.Y. Park, Y.C. Kang *Bull. Korean Chem. Soc.* 30 (2009) 2729.
- [41] G.Q. Yu, B.K. Tay, Z.W. Zhao, *Appl. Phys. A* 81 (2005) 405.



## KOREAN ABSTRACT

지르칼로이-4 (Zircaloy-4) 와 중수소화 에탄올의 표면 화학을 190K 에서  $C_2D_5OD$  의 노출량을 다르게 하여 연구하였다. TPD 실험에서는 중수소가 두 개의 다른 탈착 온도에서 넓은 탈착 스펙트럼을 동반하면서 나타났으며, 그 중 낮은 온도인 520K 에서는 일차 탈착 반응을 나타냈으며, 더 높은 온도인 650K 에서는  $C_2D_5OD$  의 노출량이 증가할수록 피크가 낮은 온도 쪽으로 이동하였다. AES 실험을 통해서도  $C_2D_5OD$  를 300 L 노출시킨 뒤, metallic 한 지르코늄이 산화가 되었음을 알 수 있었고, 단계적인 가열을 통해 산화된 Zry-4 가 다시 metallic 한 지르코늄으로 환원되었다. 가열 온도가 843K 에 이르자 산소의 양은 다시 깨끗한 표면 상태의 수준으로 되돌아갔지만, 탄소의 양은 변화가 없었다.

전기방사법으로 얻어진 고분자 나노화이버에 솔-젤 코팅법을 이용하여 타이타니아 나노화이버를 합성하고, 가열 방법을 달리하여 순수한 anatase 또는 rutile 상을 얻을 수 있었다. 두 세라믹 나노화이버들의 평균 직경은 200 nm 정도였으며, 광전자 분광기를 통해 상 변화에 따른 내각 전자 에너지 (Ti 2p) 의 차이는 없음을 알았고, valence band 에너지의 차이를 확인해 볼 수 있었다.

알루미늄 산화물이 도핑된 아연 산화물 나노화이버를 솔-젤 방법과 전기방사법을 통하여 합성하였다. 합성한 나노화이버의 직경은 60~150 nm 범위임을 확인할 수 있었고, 알루미늄 산화물의 첨가가 아연 산화물 나노화이버의 결정 크기를 작게 한다는 것을 확인할 수 있었다. 알루미늄

산화물이 도핑된 아연 산화물 나노화이버는 아연 산화물 나노화이버에 비해 낮은 밴드갭 에너지를 가졌으나, 알루미늄 양이 증가할수록 밴드갭 에너지가 증가하고 낮은 전도도를 가졌다. 전기 전도도의 변화가 도핑된 알루미늄의 양, 즉, 알루미늄의 산화상태에 영향을 받음을 광전자분석기를 통해 알 수 있었다.

스퍼터링 방법으로 soda-lime glass 에 증착시킨 Mo 박막을 광전자 분광기로 분석하였다. 스퍼터링 기체로 이용된 아르곤 기체의 압력이 증가할수록 표면의  $\text{Mo}^0$  비율은 감소하였으며  $\text{Mo}^{6+}$  의 비율은 증가하였음을 알 수 있었다. 또한 substrate 으로부터 나온 Na 도 증착된 Mo 박막의 표면에서 검출할 수 있었다.

RF magnetron sputtering 방법을 통해 산소의 양을 변화시키면서 지르코늄 산화물 박막을 Si(100) 웨이퍼에 증착하였다. 증착된 지르코늄 산화물 박막의 두께를 SE 를 통해 측정하였고, 표면의 거칠기를 AFM 을 통해 확인해 볼 수 있었다. 또한 지르코늄 산화물 박막의 결정 구조를 XRD 을 통해 알 수 있었으며, 산소의 비율에 따른 표면의 산화상태를 XPS 를 통해 연구하였다.

## ACKNOWLEDGMENTS

I would like to express my gratitude to all those who gave me the possibility to complete this thesis.

First of all, I want to thank my advisor, Prof. Yong-Cheol Kang for his continuous teaching, support throughout my undergraduate and 3 years of graduate days. I would like to extend my gratitude to all my thesis committee members, Prof. Ju Chang Kim and Prof. Prof Sang Yong Pyun, for their helpful comments and encouragement.

I want to thank Se Won Jung and Mi Sun Chun for yours help and sharing lots of precious times. I also thank Jin-Kook Heo for helping my experiment and my junior, Jun-Mo Jo for all his assistance.

I am deeply indebted to Prof. Ramsier from the University of Akron whose supported me in my research work. I would like to thank Theresa and Ann for help me adapt to Akron easily and make me enjoy the time in there. I would deeply appreciate to family of Prof. Kang, Prof. Il-Woon Kim and his wife, Jinwon Kim, and Suk Ju Kim.

I thank my lifelong friend: Yong Sun Yoo, faithful friends: Hye Joo Kang, Sun Mi Yoon, Yun Hee Lee, special friends: Mikyoung Bae, Jung Won Lee, Nam Gue Kim, Hak-Sung Jung, Hyeonsil Shin, Jung-Ae Kim.

Especially, I would like to give my special thanks to my parents for their endless love and support to complete this work.

